Applied Thermal Engineering 236 (2024) 121925

Contents lists available at ScienceDirect

Applied Thermal Engineering

journal homepage: www.elsevier.com/locate/apthermeng

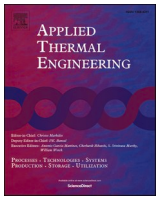

Research Paper

A New Approach of Solidification Analysis in Modular Latent Thermal Energy Storage Unit Based on Image Processing

Rafał Andrzejczyk [a], Muhammad Saqib [a,*], Michał Rogowski [a]

[a] Institute of Energy, Faculty of Mechanical Engineering and Ship Technology, Gdansk University of Technology, Narutowicza 11/12, 80-233, Poland

ARTICLE INFO

Keywords:
Solidification
Shell and Tube TES
Solid Fraction
Image processing
Front thickness
Analytical model

ABSTRACT

The solidification process of RT18HC in a cylindrical shell and tube storage unit has been studied using a new methodology based on image processing. The main idea of the algorithm is to label the region of solidification and use statistical functions to calculate the dimensions of the solidification front over time. Said analysis includes two methods. The first method is to measure the solid fraction changes during solidification. The novelty of this method, as compared to other literature findings, is that pre-processing and calculation process occurs automatically via a calculation algorithm. This method is used to calculate the solid fraction of RT18HC which is reported to be a bit fast at the beginning that 40 % of its volume solidified in 1000 s while the rest of the process is completed in almost 6500 s. The second method is used to measure and calculate the thickness of the solid front by using image processing. This method's error is calculated to be less than 7% throughout the entire process. The second method also acts as an experimental database of front thickness to use in a novel, simplified, semi-theoretical model proposed to calculate the solid front thickness as a function of time in this paper. It is also worth presenting solution extended by a general definition of thermal resistance for a cylindrical partition. The above study will enable the development of an enhanced and optimized model for complex geometries based on image processing techniques in the future. It will also allow the investigation of both processes i.e. solidification and melting alongside other influencing parameters such as the geometry of the storage unit in future.

1. Introduction

Melting and solidification phenomena occur during heat transfer associated with the phase change process and they occur not only in natural phenomena such as freezing and melting of water but also in several industrial thermal storage unit applications. Viskanta's [1] and, Cheung's and Epstein's [2] studies are some examples of scientific fundamentals of the above-mentioned phenomena. These fundamentals provide a strong basis for PCMs to be considered significant for a wide range of heat transfer applications such as thermal energy storage, power generation and solar heat storage etc. [3,4]. Moreover, this domain also got considerable attention in recent years due to a significant rise of primary energy consumption and some serious environmental concerns in future [3].

A latent heat thermal energy storage system (LHTESS) is considered to be one of the most effective mechanisms used to stimulate the phase change materials (PCMs) which leads to melting (also called heat storage or thermal storage charge) and solidification (also called heat retrieval or thermal storage discharge) [5]. Experimental results indicate that solidification occurs in a slower manner than melting. It is due to the fact that solidification is dominated mostly by conduction while during the melting process convection remains dominant [6]. However, natural convection cannot be omitted and its presence at the beginning of the process is also emphasized by some studies, and it is found effective in a horizontal annular system [7].

Melting and solidification phenomena are of great importance because of their significant role in thermal energy storage. Several experimental, numerical, and analytical studies were carried out to investigate the solidification and melting of PCMs at a wide range of temperatures and various geometrical configurations in thermal energy storage units [3]. For example, an approximate analytical model has been developed by Lamberg et al. [8] to study a two-phase solidification problem. Estimation of solid–liquid interface and fin temperature calculated satisfactorily by the developed analytical model with a 10 % error of a solid fraction of PCM. Mosaffa et al. [9] also investigated a two-dimensional solidification problem analytically in a shell and tube heat exchanger having a radial fin. Rectangular storage units and cylindrical shells with similar heat transfer surface area and volume were used to study the solid fraction of PCM. This indicated that the

* Corresponding author.
E-mail address: muhammad.saqib@pg.edu.pl (M. Saqib).

https://doi.org/10.1016/j.applthermaleng.2023.121925
Received 5 June 2023; Received in revised form 19 October 2023; Accepted 3 November 2023
Available online 4 November 2023

Nomenclature

D	Diameter (m)
Fo	Fourier number
h	Latent heat of fusion (kJ/kg)
m	Mass (kg)
$\dot{m}$	Mass flow (kg/s)
R	Radius (m)
Ra	Rayleigh Number
Ste	Stefan number
t	Time (s)
T	Temperature (K)
W	Width (m)
α	Thermal diffusivity (m^2/s)
β	Coefficient thermal expansion (1/K)
ε	Ratio of substitute thermal conductivity and average thermal conductivity (-)
λ	Coefficient of thermal conductivity (W/mK)
ρ	Density (kg/m^3)

Abbreviations

HTF	Heat transfer fluid
LHTESS	Latent heat thermal energy storage system
MAE	Mean absolute error
PCM	Phase change material
PSNR	Peak signal noise ratio
RMSE	Root mean square error
SHTESS	Sensible heat thermal energy storage system
SNR	Signal-to-noise ratio
TEES	Thermal energy storage system
TES	Thermal energy storage
UQI	universal quality index

Subscripts

s	solid phase
i	initial
in	inside
d	dark region (shadow)
k	thermal conductivity
sh	shell
t	tube
w	wall
ch	characteristic

solidification process was quicker in a cylindrical shell as compared to a rectangular one. Al-obaidi used a very interesting geometry of three-dimensional circular pipe with twisted tape and study the thermal flow, heat performance analysis and heat enhancement using experimental and numerical approaches [10–13]. This geometry could be incorporated in thermal energy storage units.

A multi-tube LHTESS containing two PCMs i.e., RT35 and RT50 is used in [14] to study the solidification process. Results indicated a simultaneous solidification in each section. Another multi-tube LHTESS study was done by Esapour et al. [15] using RT35 as PCM. They achieved the highest melting time and shortest solidification time by locating four tubes within the storage tank. Loem et al. [16] performed a thermal analysis of RT18HC for energy-saving purposes in air-conditioners and reported a 13.8% saving of energy at certain parameters. Another comparative study was done by MH Jahangir et al. [17] using different PCMs from the RT group to study the thermal performance of air base thermal/photovoltaic system and concluded that RT18HC shows an increment of 1.71% as compared to other PCMs. They also studied the effect of PCM layer thickness and reported 120 mm as the optimum thickness of PCM for a given system.

Besides the above-mentioned research, several studies have been reported on the melting and solidification processes of PCMs in literature [3,18] and such parameters as liquid and solid fractions were also their point of investigation, as an indicator of the speed of the process. Generally, to track the solid–liquid interface a few different methods have been reported in the literature. Wang and Fautrella [19] reported utilizing thermocouples, while Gardent and Salvi [20] demonstrated the resistance system to measure the movement of the interface what is more also ultrasound techniques could be used to measure the thickness of each phase. However, both the resistance and the ultrasound techniques are possible to use in the case of metallic PCMs (e.g., Gallium) [21]. It seems that the X-ray visualization method is a more universal technique with high accuracy. This technique is based on mass absorption. The change in the density of a substance caused by a phase transformation from liquid to solid, commonly of the magnitude of at least 2%, results in a change of transmitted intensity of the X-ray beam. Still, that kind of methodology is rather commonly used in the case of metallic PCM with a much large density than in the case of organic ones [22].

Numerical methods are also used for mapping of solid–liquid interface and calculation of liquid fraction. Assis et al. [23] performed experimental and numerical investigations on the melting of RT27 (Rubitherm GmbH) under a constant wall temperature boundary condition (Ste $<$ 0.2). The convection in the liquid phase, the volumetric expansion due to melting, the sinking of the solid in the liquid, the close contact melting, and the thermal resistance of the test shell by the transient numerical solution were conducted using FLUENT software. The Nusselt number and the liquid fraction are presented in terms of the Fourier number, the Stefan number, and the Grashof number by dimensional analysis. Shmueli et al. [24] carried out a numerical investigation on the melting of Rubitherm RT27 in a vertical cylindrical tube. The effect of the mushy zone constant, the influence of the pressure velocity coupling, and the pressure discretization scheme on liquid fraction variation is examined. The authors observed that the results were extremely sensitive to the value of the chosen mushy constant (10^5 – 10^10). Pinelli and Piva [25] reported a numerical investigation of the melting of n-octadecane heated from above. Results show that the consideration of natural convection leads to a significant improvement in the agreement between numerical results and experimental data.

However, in very few studies, the effects of the thickness of solidification front were investigated and explained without devising a proper theoretical model [26,27]. The mentioned studies developed a simplified model to measure and calculate the solidification layer thickness as a function of the time using water as a PCM. They determine the influence of solidification layer thickness on the solidification process along with the effect of the contact layer and its dependencies on solidification layer thickness. This gave authors a motivation to analyze the solidification process using some novel methodologies based on image analysis/processing and propose a novel technique to measure and calculate not only the solidification layer thickness but a solid fraction too. This study will also lead authors to develop a more sophisticated and universal model based on image processing techniques in the future.

As mentioned above, the motivation and intention to present this paper is the adaptation of a novel methodology based on image analysis to calculate the solid fraction and analyze the solidification process of RT18HC in the shell and tube storage unit. There are very few studies published in the past 5 years (see Table 1 [28]) that claim to use image analysis or claim to partly incorporate visual analysis for validation purposes. However, there was one study by M. Azad et al. [29] found in the literature up to the best knowledge of authors which describes using

Table 1
No of Paper published using image analysis/processing [28].

Year	2019	2020	2021	2022	2023
No. of published papers	3	2	8	4	3

image processing to calculate the solid fraction. The authors of said article studied the solidification process in horizontal annulus and obtained the solid/liquid volume of PCM per unit length photographically or we can say through image analysis but in a whole different scenario and parametric conditions.

The following study, however, focused on vertical shell and tube storage. The authors did not only obtain solid fraction as a function of time but also the solidification front thickness, which was calculated in an attempt to overcome the issue of the non-availability of data regarding solidification front thickness in the literature. Following it a novel simplified semi-empirical theoretical model has been proposed to calculate the solidification front thickness as a function of time. What is more, the presented technique is more universal than in the case of other non-invasive methods presented in the literature.

2. Experimental setup

The experimental loop presented in Fig. 1 consists of two sub-loops: a primary one and a secondary one. These two loops are coupled with a common plate heat exchanger (7). The primary section was designed to obtain large temperature differences between the inlet and outlet to the heat exchanger (7), which serves the purpose of evaluating heat transferred from an experimental section (1). Both sub-loops use the same HTF – distilled water. Heat, which needed to be received for PCM to undergo the solidification process in experimental module (1), was absorbed by cold water supplied from an ultra-thermostatic bath (2), which consists of a Julabo's CORIO CD electric thermostat and an S&A's SW-5300 Industrial Chiller. In both of these appliances, the temperature is controlled by the electronic, precise temperature control system.

Primary circuit HTF flow is provided by a Julabo's CORIO CD built-in circulation pump. The required level of flow in the primary circuit is controlled in the overflow vessel (6) by its control valve. Liquid flow is split into two parts inside an overflow vessel (6), one part flows through the heat exchanger (7) and collecting vessel (8), while the surplus is being returned back to the ultra-thermostatic bath (2). The collecting vessel (8) is equipped with a three-way valve, which allows for a normal flow into the ultra-thermostatic bath (2) or redirection of the flow into a beaker put on a STEINBERG's SBS-LW precision scale. Measurements the of mass of the HTF within a certain period of time allow for the evaluation of the mass flow rate. The temperature of the HTF at the inlet and outlet of the heat exchanger (7) is measured with 4-wire, class A, Pt100 resistive temperature sensors.

The secondary loop of the experimental test section serves the purpose of retrieval of heat stored in PCM within the experimental module (1) while maintaining constant wall temperature on the wall of the working element (a copper pipe). To meet this criterium, the highest possible HTF flow was obtained using KPER 63 K2 [VEM] gear pump (11), while the water meter (12) indication after calculations controls the volume flow of the secondary loop's HTF. HTF temperature on the inlet and outlet of the experimental module (1) is measured using 4-wire, class A, Pt100 resistive temperature sensors. A secondary loop was additionally equipped with a safety group composed of a diaphragm expansion tank (2), safety valve (3), automatic air vent (4), and a control pressure gauge. HTF then flows through the heat exchanger (7) in which it is cooled. Temperature distribution within the experimental module (1) is measured using 15 T-type thermocouples, and 4 class A, 4-wire Pt100 resistance sensors. All of the mentioned temperature sensors are connected to the National Instruments' NI eDAQ-9189 data acquisition system (18) equipped with two NI-9212 thermocouple modules. This system is connected to a lab computer (19) running a LabVIEW graphical programming tool allowing for data acquisition. The uncertainties of the measured parameters are given in Table 2.

Temperature distribution within the experimental module (1) is also controlled using Flir C3 thermal imaging camera (15). The optical

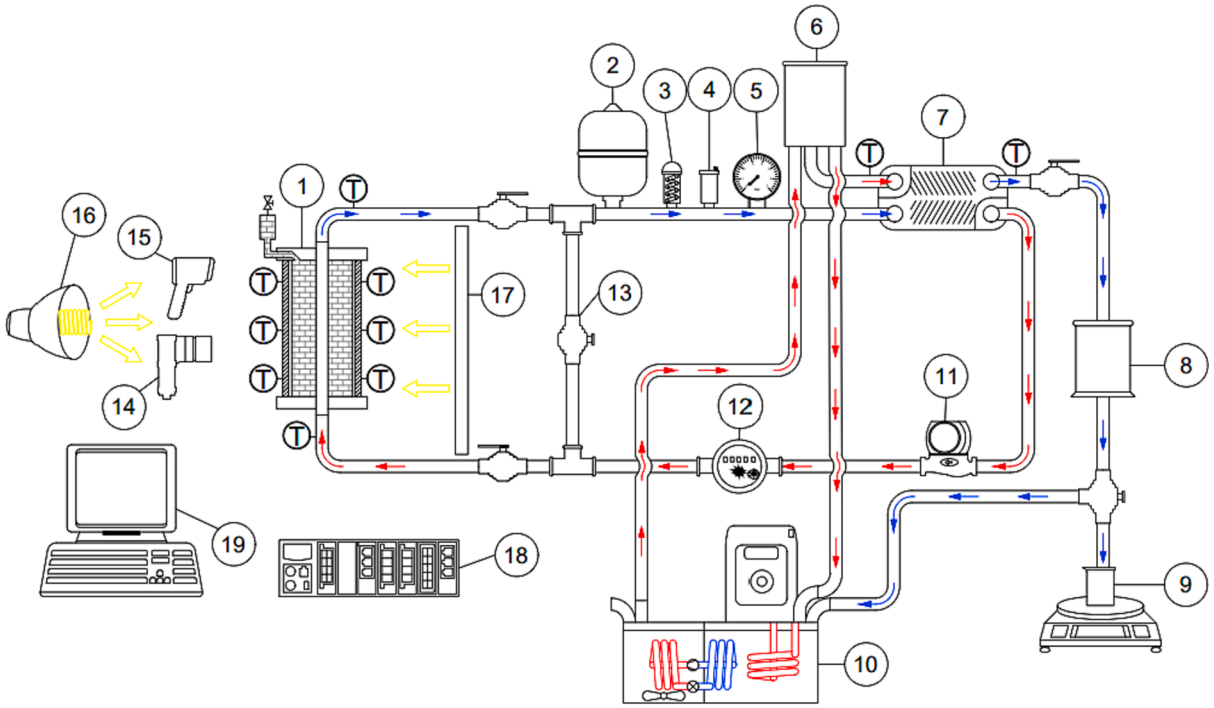

Fig. 1. Schematic view of experimental test section; 1 – PCM-filled experimental module with filling attachment, 2 – diaphragm expansion tank, 3 – safety valve, 4 – automatic air vent, 5 – pressure gauge, 6 – overflow vessel, 7 – plate heat exchanger, 8 – collecting vessel, 9 – beaker on a precision scale, 10 – ultra thermostatic bath, 11 – variable flow pump, 12 – water meter, 13 – by-pass, 14 – industrial camera with lens, 15 – infrared camera, 16 – light illumination, 17 – light-reflecting wall, 18 – NI DAQ system, 19 – lab computer.

Table 2
Uncertainties of measured parameters.

Parameter	Operating range	Uncertainty
T_{PCM}	283.15 K – 333.15 K	±0.3 K
T_w	283.15 K – 333.15 K	±0.05 K
M	260–360 g	±0.1 g
m	8.63–11.27 g/s	1.2 %

Table 3
Geometric parameters and material properties of the shell and working element.

	Shell	Working element
Outer diameter [mm]	50	10
Thickness [mm]	5	1
Active length, H [mm]	165	165
Material	Acrylic glass (PMMA)	Copper

illumination and image acquisition system consists of an IDS's UI-1220ME-C-HQ equipped with an H1214-M lens (14), a G801A light fixture with a spiral 85 W photo bulb (16), and a reflective wall (17) which allows for better illumination of the experimental module (1). Both the thermal imaging camera (15) and the photographic camera (14) are connected to the lab computer (19) equipped with custom-made photo acquisition software allowing for photo acquisition from cameras. A schematic representation of this setup is shown in Fig. 2.

The test module for the PCM solidification study was designed with the intention to capture the solidification front, thus the designed module consists of a cylindrical shell made of a transparent acrylic glass pipe with an OD of 50 mm and a wall thickness of 5 mm. To reduce heat losses, the experimental module was insulated with polyurethane. Due to solidification, the front issue shell was insulated only on the backside, on about 1/4 of the circumference. The height of the shell's active part is 165 mm. Inside the shell is a copper tube with a 10 mm OD and a 1 mm wall thickness, whose lateral surface area serves as a heat transfer surface during the experiment. Shell elements have been made from transparent acrylic glass which characterizes as a good thermal insulator, with the thermal conductivity below 0.2 W/mK and a high light transmittance of above 90%, which was one the most important parameters during the preliminary design. All of the geometric parameters and material selection of the experimental module are put in Table 3.

To measure temperature distribution within the experimental module 15 T-type thermocouples with a 1 mm jacket diameter and a 300 mm length and 4 class A, 4-wire Pt100 resistive thermometers with a 1.5 mm jacket diameter and a 150 mm length were used. The sensors were arranged on 5 surfaces (S) and 4 radiuses (R) from the axis of the experimental module, called respectively S1, S2, S3, S4, S5 and R7, R10, R13, and R16. The heights of the surfaces and radiuses of temperature sensors are shown in Fig. 3. The values of radiuses for R7, R10, R13, and R16 are respectively: 7 mm, 10 mm, 13 mm, and 16 mm. The arrangement of specific temperature sensors is shown in Table 4.

2.1. Thermodynamic properties of PCM (RT18HC)

RT18HC was selected as a PCM in the following study. It should be noted that this substance has the same melting point as glycerol, i.e. 291.15 K (18°C), it is also organic and biodegradable. As in the case of the other PCM substances considered. There is not much literature data available on the thermal properties of the PCM under consideration. However, the thermal properties mentioned in Table 5 were taken from the manufacturer's website [30].

In the case of the dynamic viscosity measurements, a Vpad's Rotational Viscometer with an indication accuracy in the range of ±1% was used. It should be noted, however, that the target accuracy can be obtained for the best value of spindle speed and sensor type. Dynamic viscosity examination for RT18 HC was carried out in a narrow temperature range to obtain results with the least possible errors. The dynamic viscosity value varies between 0.0045 and 0.049 Pa*s. Comparing the obtained results, despite the unknown temperature for which the authors of the work obtained the value, with the literature data, it can be concluded that they are close to each other [31]. Larger discrepancies appear below temperatures of 290.95 K (17.8°C). This undoubtedly indicates the beginning of the phase transition (medium concentration) at this temperature.

Reliable dynamic viscosity characteristics for RT18HC require the use of a wider range of measuring sensors with simultaneous attempts to optimize the number of spindle revolutions per minute so that the obtained results are not burdened with thick errors. These errors may occur when measurements are carried out outside the range of a dedicated sensor at a certain rotational speed. In the case of this substance, it is necessary to perform measurements in a narrow temperature range, in particular in the temperature range in which the phase transition

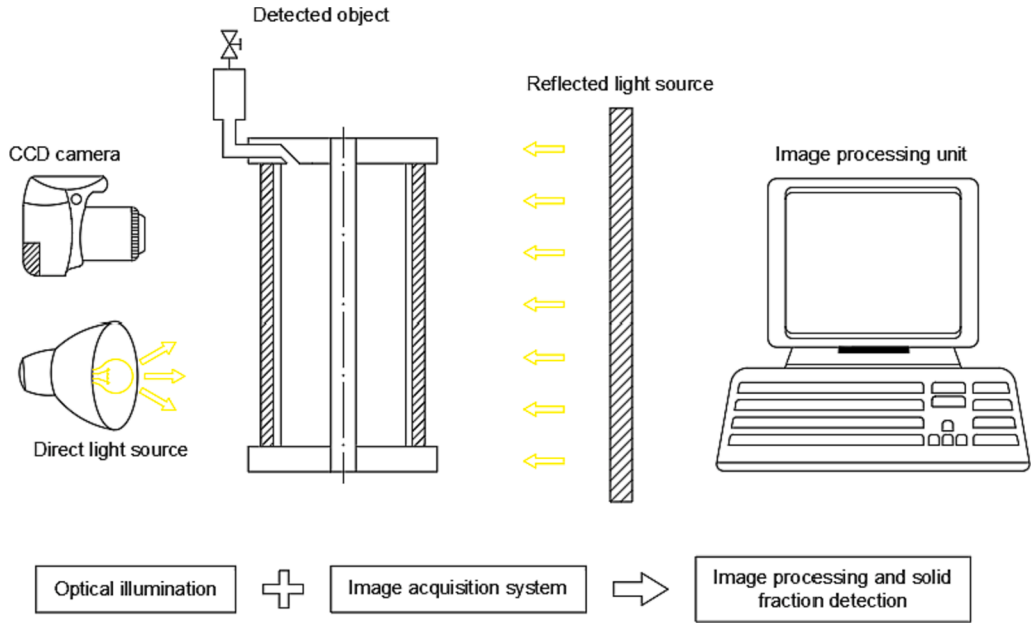

Fig. 2. Schematic representation of existing light sources in the experimental test section and image-based solid fraction detection model.

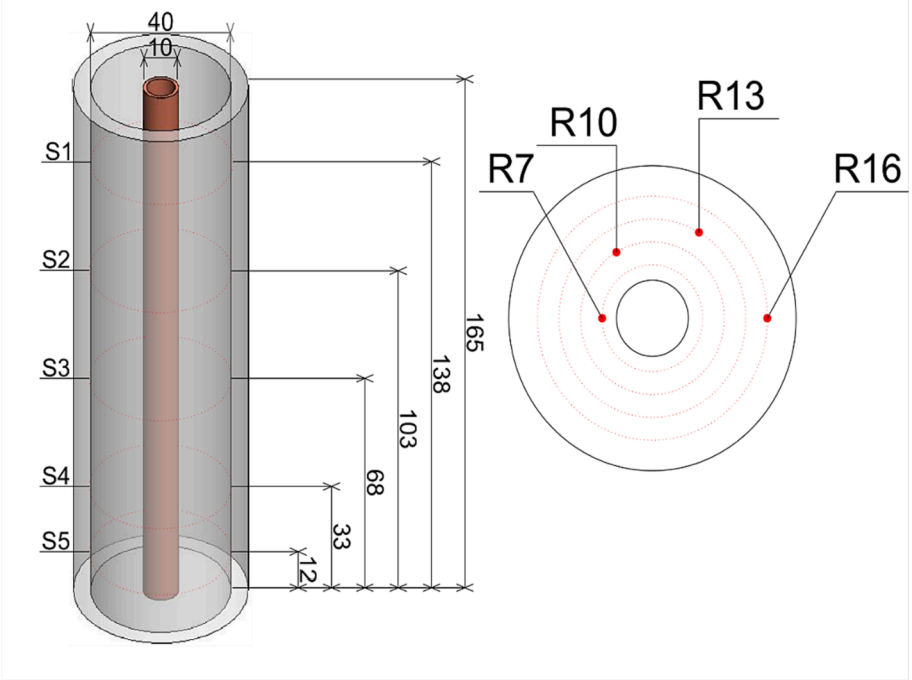

Fig. 3. Temperature sensors arrangement at certain heights (S1, S2, S3, S4, S5) and radiuses (R7, R10, R13, R16).

Table 4
Temperature sensors arrangement within the experimental module.

Surface of temperature sensor	Radius of temperature sensor location			
	R7	R10	R13	R16
S1	T12	T8	T4	T0
S2	T13	T9	T5	T1
S3	T14	T10	T6	T2
S4	T15	T11	T7	T3
S5	T19	T18	T16	T17

Table 5
Selected thermophysical properties of RT18HC [30].

Property	Unit	Value
Melting point	K	290.15–292.15
Pour point	K	292.15–290.15
Latent heat of fusion,h_{ls}	kJ/kg	260
Solid phase density (measured at 288.15 K),ρ_s	kg/l	0.88
Liquid phase density (measured at 298.15 K)ρ_l	kg/l	0.77
Thermal conductivity (both liquid and solid), λ	W/mK	0.2
Ignition point	K	408.15
Maximum operating temperature	K	323.15
Volume Expansion	%	12.5

process is expected.

3. Thermal analysis of experimental results

Temperature profiles obtained in individual planes are characteristic for phase-change substances that do not show supercooling effect [32]. As in the case of RT18HC, during solidification, a variation in the cooling rate of the substance is observed depending on the distance from the heat exchange surface. In other words, temperature profiles of all surfaces predict an almost similar decreasing trend of temperature (see Fig. 4, Fig. 5 and Fig. 6). A sharp decrease in temperature can be seen on inner radius R7 i.e. near the tube for all surfaces which predicts a faster solidification rate near the tube and a slower rate in outer radii R10, R13, and R16 on each surface. This can be explained by thermal resistance caused by solidified PCM layer around the tube. It affects the heat transfer process strongly and impedes the heat transfer from the heat transfer surface to the liquid fraction. This effect is the deterioration of the natural convection influence on heat transfer. The heat transfer is dominated by the conduction mechanism. What is more due to the low value of PCM conductivity the crucial parameter is the distance between PCM and heat transfer surface. Undoubtedly temperature profiles presented by sensors T16, T17, T18, and T19 have been affected by the ambient conditions. It should be noted that due to technical problems some sensors could not be bent (see Fig. 7 and Fig. 8).

4. Image analysis

4.1. Image processing

The new method of solid fraction measurements by image data analysis has been carried out. In this analysis, the main focus has been placed on image pre-processing. First of all, the quality of the photos has been checked to confirm the usefulness of the database of the image. Image quality is a crucial parameter in image processing applications. The most popular class of objective quality distortion is the mathematical one. In this method parameters such as MSE (mean square error), PSNR (peak signal noise ratio), RMSE (root mean square error), MAE (mean absolute error), SNR (signal-to-noise ratio), UQI (universal quality index) needs to be calculated. The calculation methodology was based on MATLAB code from the literature [33]. The results (see Fig. 9, Fig. 10 and Table 6, Table 7 respectively) have shown a good quality image database. It is confirmed that the noise influences at the presented image database were not significant. It is spatially important for presented methodology which is based on binary images. The large fluctuation of random brightness or chromatic aberration could disqualify the valence of image base to use in image data analyzing procedure to calculate the geometrical parameters of phase change front.

4.1.1. Pre-processing of the images

The three kinds of filtration for each photo have been analyzed (see Fig. 11). The human perception of the quality of photos is not always met with the best photo quality. Due to that fact, finally, the MATLAB

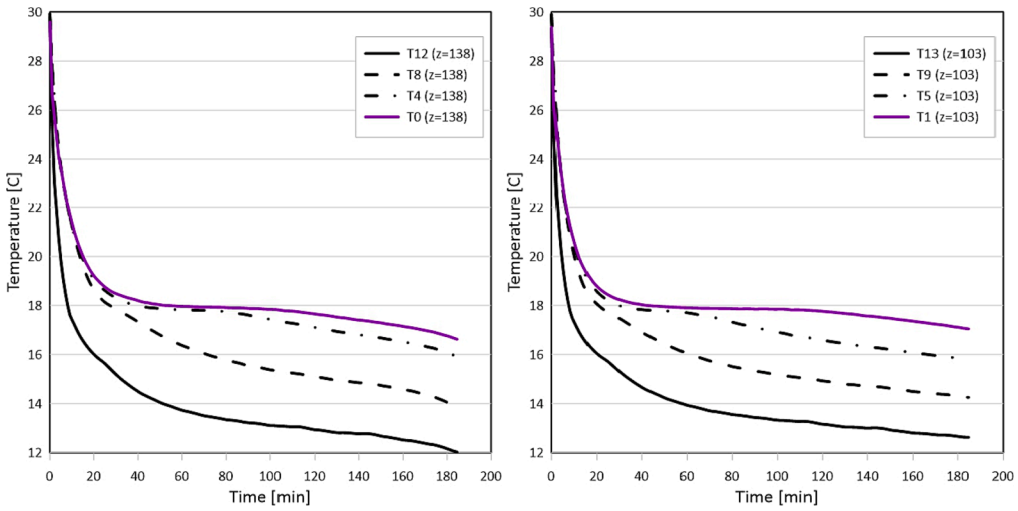

Fig. 4. Temperature profile for solidification of RT18HC for constant wall temperature (T_w = 10.5C): on the left surface S1; on the right surface S2.

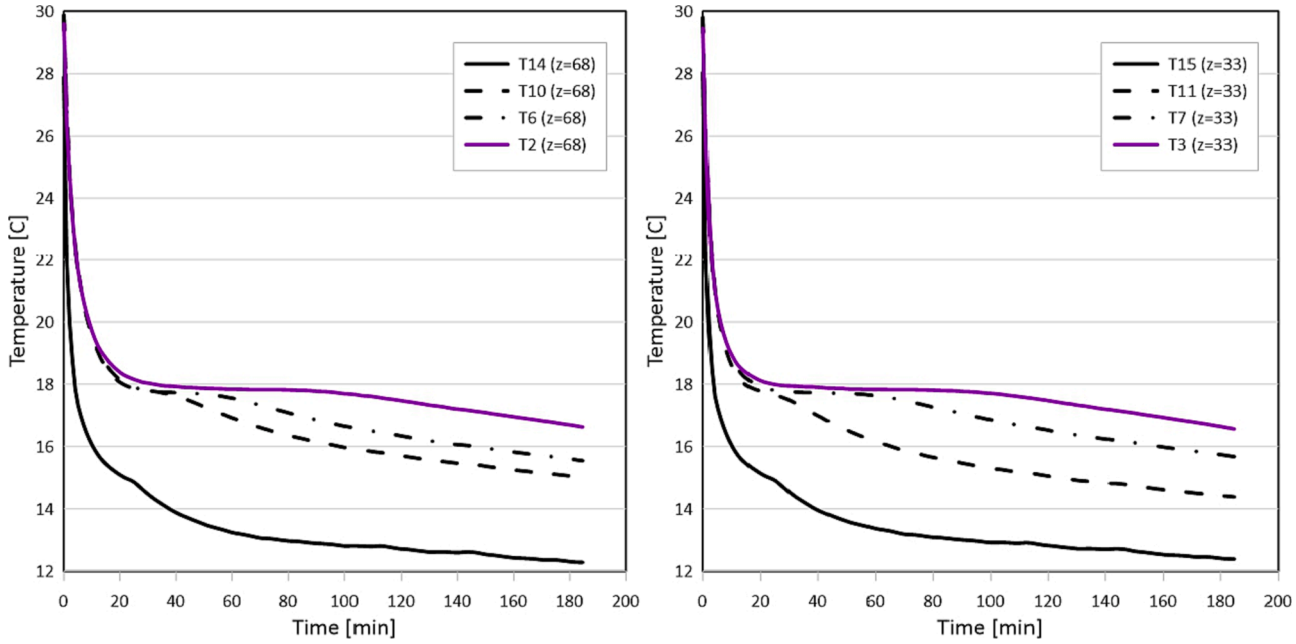

Fig. 5. Temperature profile for solidification of RT18HC for constant wall temperature (T_w = 10.5C): on the left surface S3; on the right surface S4.

function of the Natural Image Quality Evaluator was used to judge the filtration.

To measure the solid fraction changes during the solidification process two different methods have been used. Both of them use images only in black and white color scale (binary image). It is due to the fact that RT18HC in the solid phase has an opaque white color which transforms to transparent liquid upon melting. At first, all photos were changed from RGB scale to grayscale and then to binary image. In such a case, the solid fraction was matched as white, and the liquid as black (Fig. 12).

In connection with this approach, the influence of disturbing factors on the measurement should be taken into account. One of the main factors was the gradient shadow pattern. This shadow is created by the temperature sensors immersed in the PCM inside the experimental module. However, due to a diminishing effect most of the sensors have been bent. Only sensors placed at the last (bottom) surface were not bent because of limited space. Those elements created the largest disruption (see Fig. 14).

Another disruption is the results of illumination conditions and optical properties of experimental module material as well as PCM material. In this context, the most important parameter is the refractive index, which is a fundamental property of a substance that determines the path light takes as it crosses the interface between two media. According to the literature in such systems like in the following article, the relation between illumination conditions and cylindrical geometry as well as filling the volume of shell substance created the area of the dark at the cylinder border (see Fig. 13).

Knowing the refractive index for the experimental module material (PMMA) and the PCM material it is possible to estimate the width of shadowing areas [34]. It should be highlighted that there is a literature gap for the refractive index for RT18HC. What is more, this a parameter is a function of temperature. To estimate the width of the shadow area it has been assumed that the refractive index for RT18HC is close as for RT21HC [35].

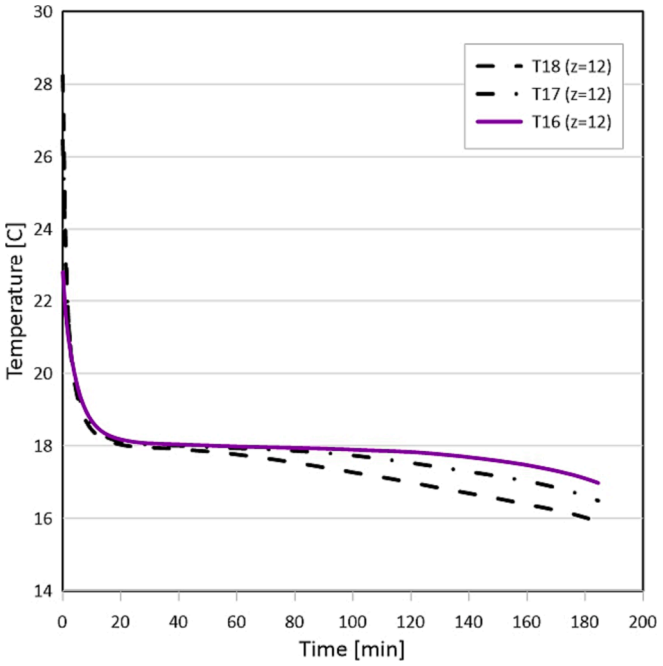

Fig. 6. Temperature profile for solidification of RT18HC for constant wall temperature (T_w = 10.5C) at surface S5.

$$W_d = \frac{D_{sh} - \left(\left(\frac{n_{PCM}}{n_{PMMA}}\right) - \theta\right) \bullet \frac{D_{sh}}{\sigma}}{2} \quad (1)$$

Where n_{PCM} was assumed as 1.435 and n_{PMMA} as 1.49, $\theta = 0.77$ and $\sigma = 0.21$. Finally, the width of the shadow could be estimated as close to 1.5 mm at the border of the system.

4.2. Experimental procedure of solid fraction measurements by first method

According to the first approach the solid fraction was calculated as the result of subtracting image by image from the same starting point (the first image in the series). In case of RT18HC the phase transformation takes place over a range of temperatures. In this temperature range both (liquid and solid phases) are present. However, it should be noted that temperature range for RT18HC is quite small (see Fig. 15). That is why to simplify the methodology it has been assumed that there is no influence of mushy zone.

The final results were presented as a percentage change amount of solid phase. It should be noted that more than six hundred photos have been analyzed, meaning the time resolution was equal to 10 s. The calculation analysis has been made by an in-house MATLAB algorithm. A similar methodology has been presented by M. Azad et al. [36]. However, there is a visible difference in the case of pre-processing of photos. In above-mentioned study [36] all photos have been manually processed in Adobe Photoshop CC. Then the images were imported into MATLAB for the rest of the procedure. In the presented approaches all procedures have been done in MATLAB. Therefore, it was possible to directly analyze phenomena in real-time, using the following equations:

$$\varphi_i = \sum_{\tau=i}(P_w + P_b) \quad (2)$$

where:

P_w– value attached to white pixels [-].

P_b– value attached to black pixels [-].

At the time point $\tau = 0$, i.e. at the beginning of melting process, the whole volume of module was filled with PCM in a solid phase:

$$\varphi_0 = \sum_{\tau=0}(P_w + P_b) \quad (3)$$

Solid fraction was then calculated using the following formula:

$$\varphi = \frac{(\varphi_i - \varphi_0)}{\varphi_0} \bullet 100\% \quad (4)$$

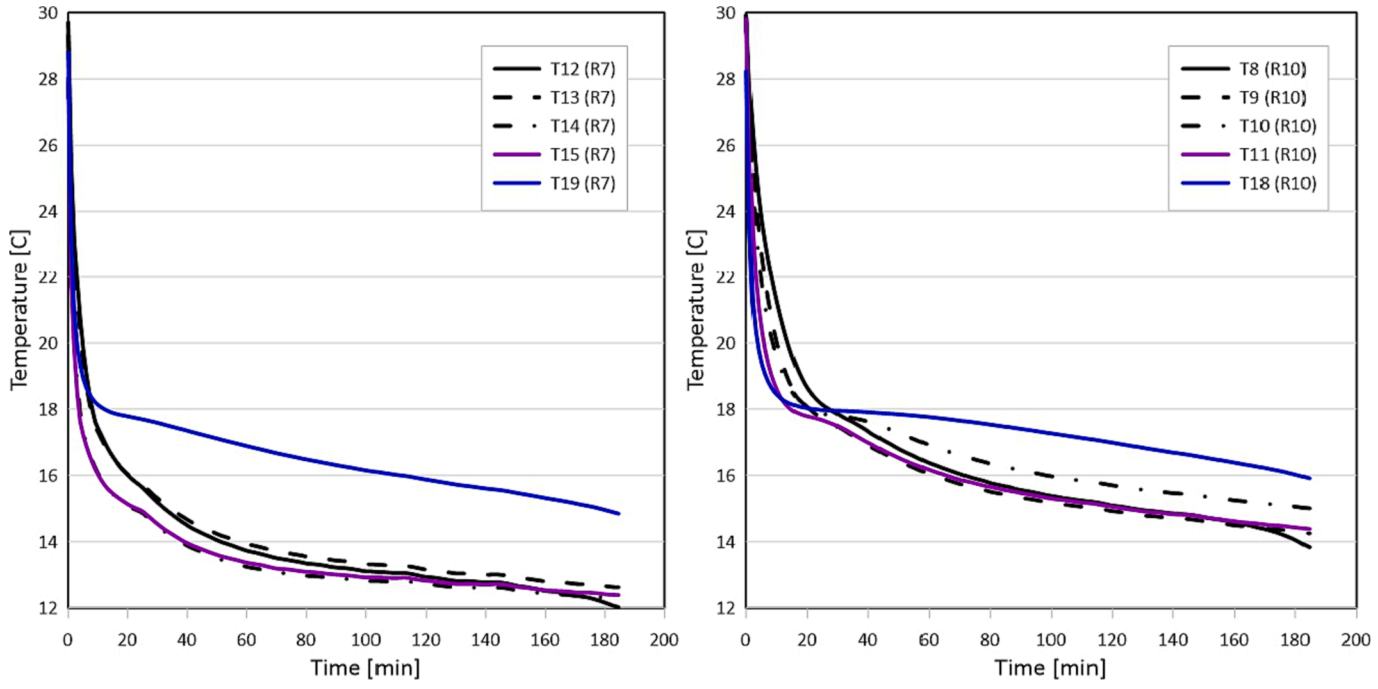

Fig. 7. Temperature profile for solidification of RT18HC for constant wall temperature (T_w = 10.5C): at left for R = 7 mm; at right for R = 10 mm.

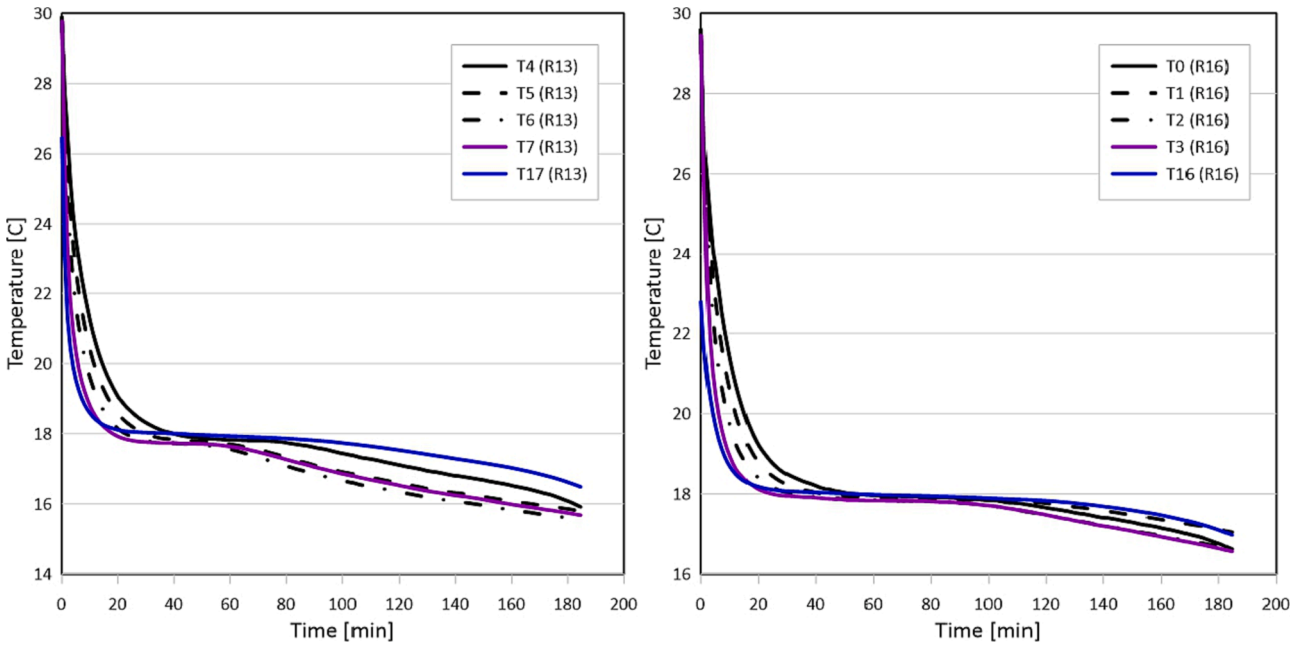

Fig. 8. Temperature profile for solidification of RT18HC for constant wall temperature (T_w = 10.5C): at left for R = 13 mm; at right for R = 16 mm.

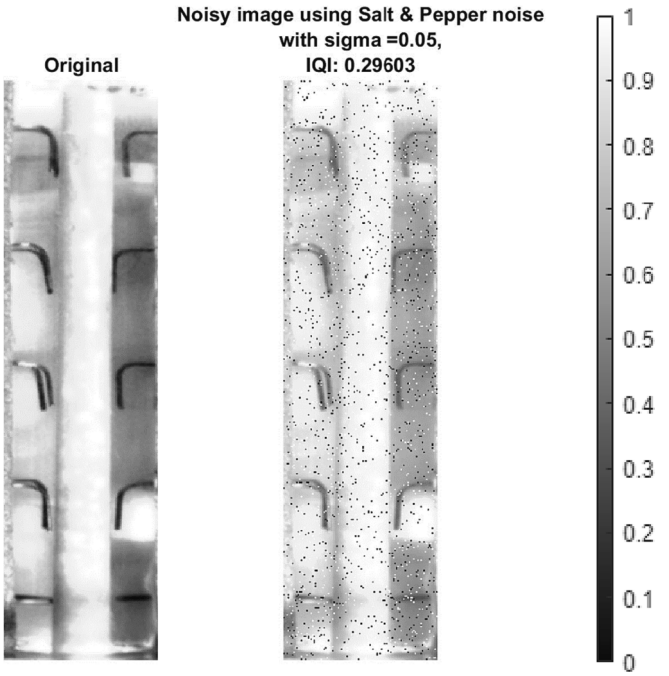

Fig. 9. Evolution of the first photo by additive noises.

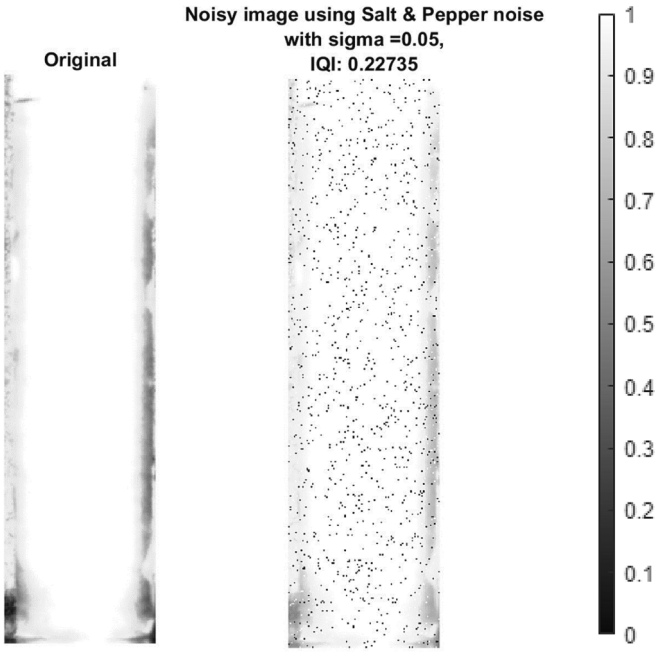

Fig. 10. Evolution of the last photo by additive noises.

Fig. 16 presents solid fraction as a function of time. It should be emphasized that at the beginning of the process, the amount of solid fraction changes rapidly. It is because of natural convection domination. A similar effect of short domination of natural convection during solidification was also observed by other authors [37,38]. Then the changing of the solid fraction behaves in a linear manner. This fact confirms domination of conduction mechanism.

Knowing the solid fraction, it is possible to calculate the amount of heat released from solidified PCM using the following formula:

$$Q = \varphi \bullet h_{ls} \bullet m_{PCM} \tag{5}$$

Where:

φ– solid fraction of PCM [%].
h_{ls}– latent heat of fusion [kJ/kg].
m_{PCM}– mass of PCM stored within the experimental module.

Heat released during the solidification process was shown in Fig. 17 as a function of time.

4.3. Experimental procedure of solid fraction measurements by second method

The second methodology is based on thermal resistance theory. By using MATLAB algorithm, it was also possible to measure the front thickness of the solidified layer over time (see Fig. 18). It should be noted that this is the novelty of the proposed technique. The main idea of

Table 6
First photo quality parameters.

PSNR	MSE	RMSE	UQI	EME (original image)	EME (noisy image)	PCC (original image)	PCC (noisy image)	SNR	MAE
+17.38 dB	1198.34	34.62	0.295	3.37	1.29	32039.35	43,739	6.72 dB	6.28

Table 7
Last photo quality parameters.

PSNR	MSE	RMSE	UQI	EME (original image)	EME (noisy image)	PCC (original image)	PCC (noisy image)	SNR	MAE
+16.39 dB	1505.26	38.80	0.230	0.50	0.07	15498.17	43739.00	−7.71 dB	6.18

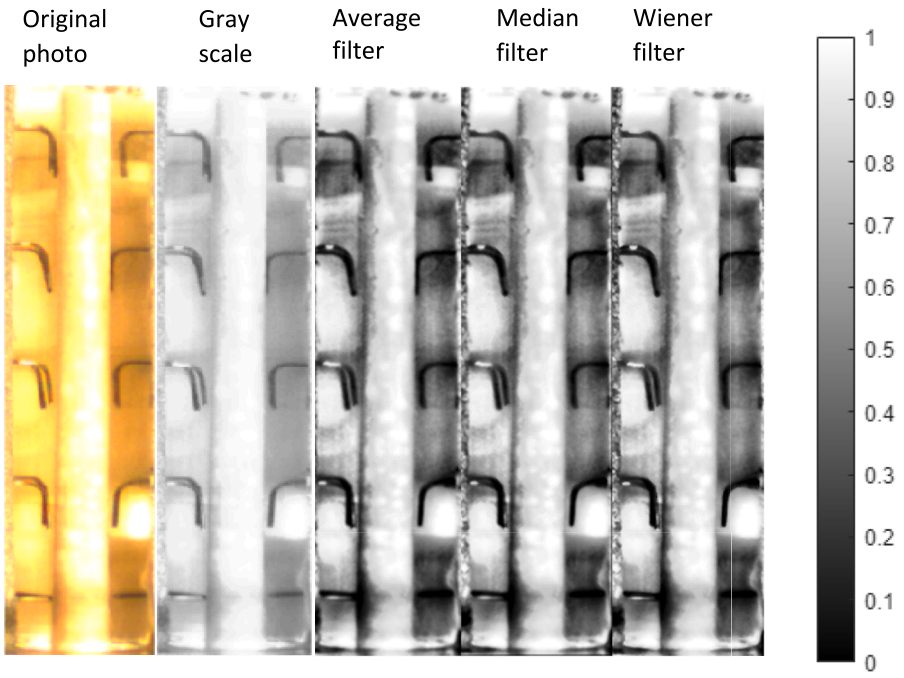

Fig. 11. Example of filtration results.

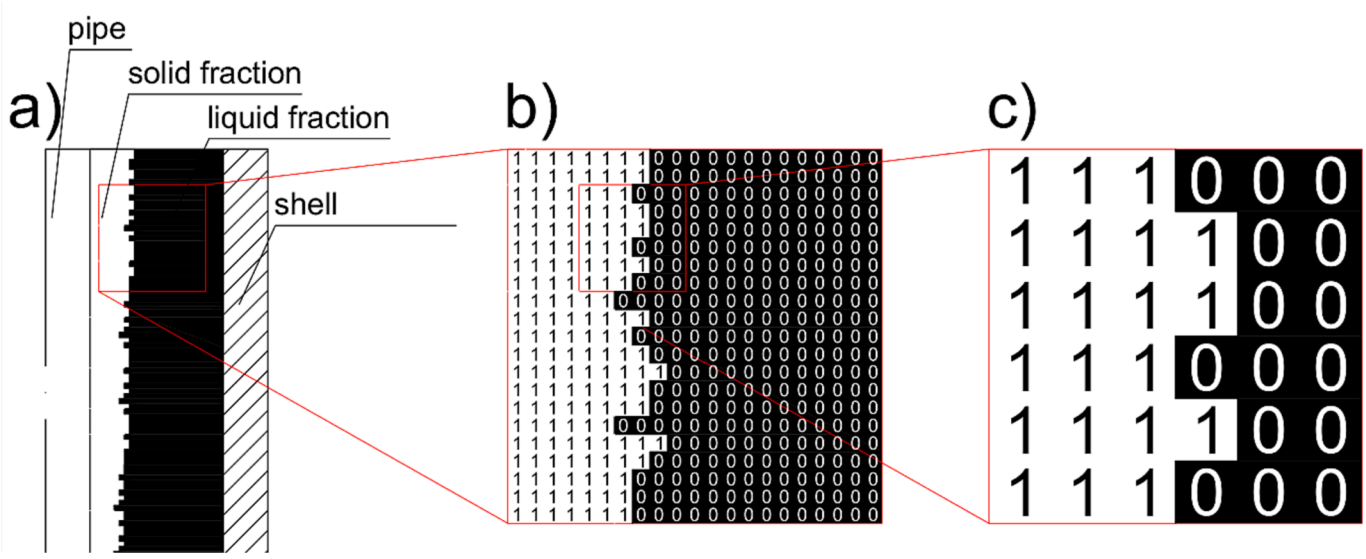

Fig. 12. Schematic representation of method: a) binary photo of cylindrical shell filled with PCM during solidification process; b), c) close-ups of certain parts of pixel map (0 – solid fraction of PCM; 1 – liquid fraction of PCM).

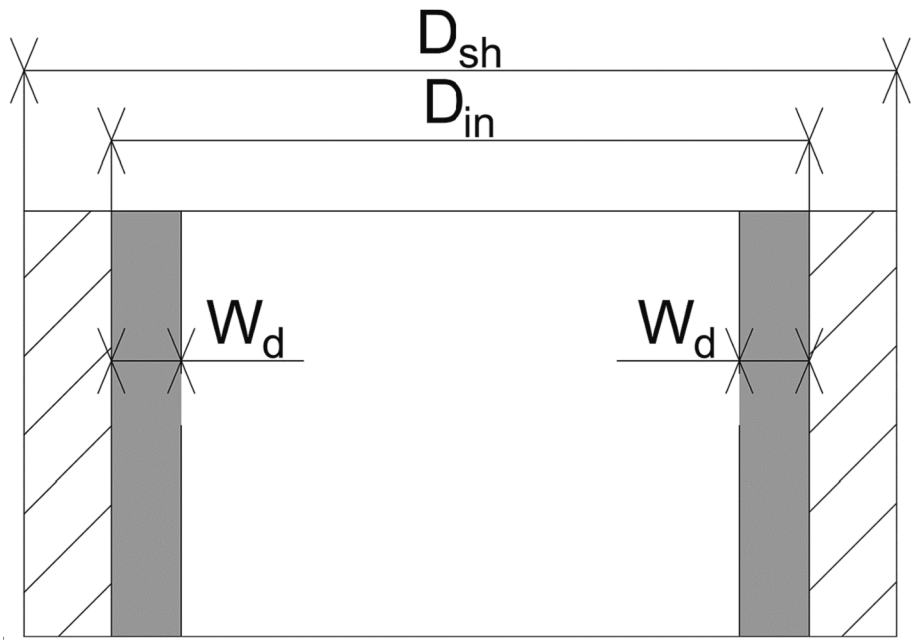

Fig. 13. Schematic representation of the dark region at the border of the experimental module's shell.

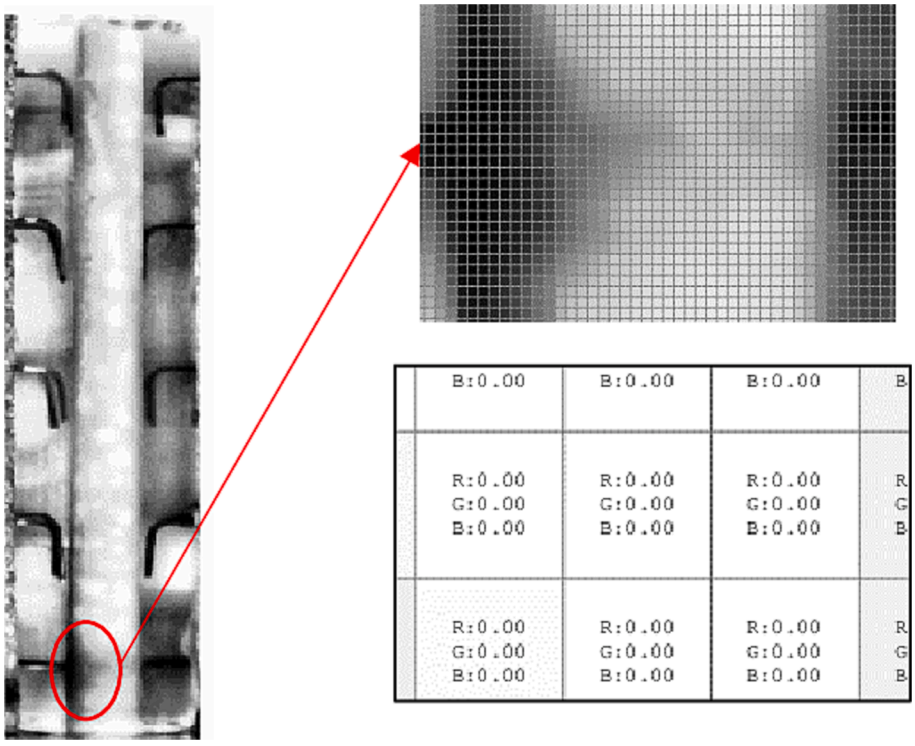

Fig. 14. Example of gradient shadow pattern resulting from temperature sensors influencing image data analysis.

the algorithm is to label the region of solidification and use statistical functions to calculate the dimensions of the solid front over time. By using MATLAB, it is possible to calculate many labelled region parameters [39]. It should be highlighted that the number of labeled regions are different and depend on changing of solid front geometry. There is also visible influence of shadows. As it was noted before these shadows are mostly created by temperature sensors mounted to the experimental module. Due to that fact the number of labeled regions are changing.

Finally, the width of the solid front has been calculated as a difference between the i-image and the first one. However, due to the disturbing image by shadow pattern, the program matched not only one region for front thickness calculations. What is more the results of the thickness were not distributed symmetrically (see Fig. 19). Furthermore, in this scenario mushy zone influences have also been neglected.

As a result of that the median value of the parameter was taken into calculation methodology.

$$\delta = w_i - w_0 \tag{6}$$

$$w = median(w_1 : end) \tag{7}$$

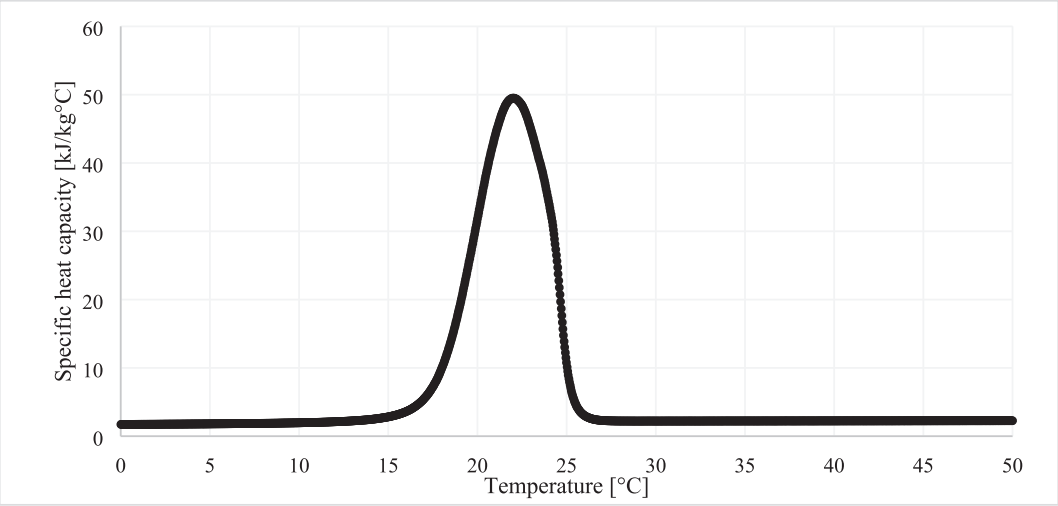

Fig. 15. Specific heat capacity of RT18HC as a function of temperature obtained from DSC examination.

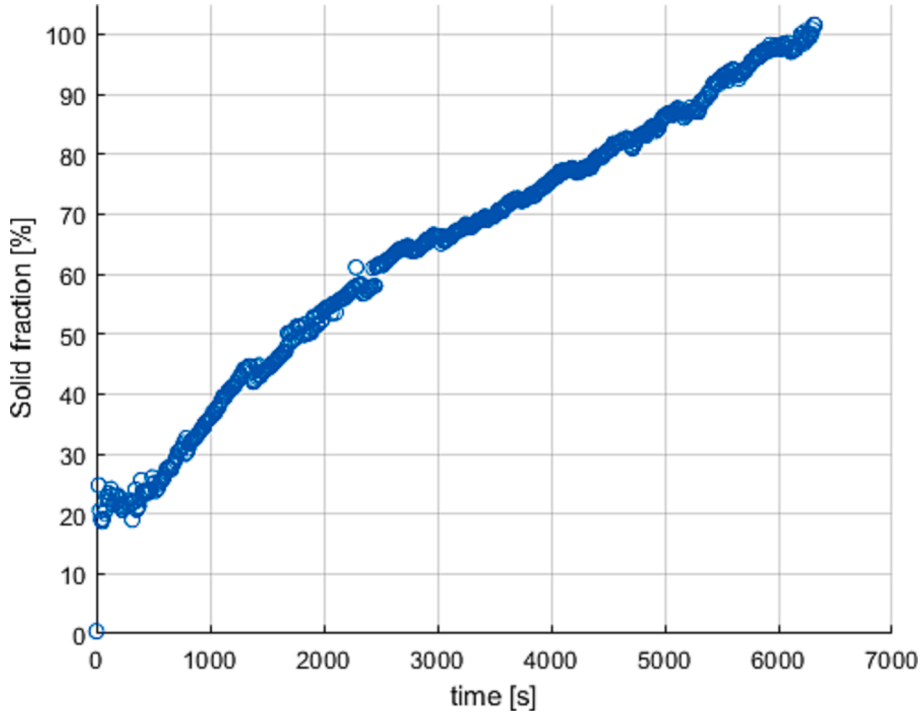

Fig. 16. Solid fraction as a time function during solidification of RT18HC.

$$d_i = d_r + 2 \bullet \delta \tag{8}$$

$$R_{cond} = \frac{\log\left(\frac{d_i}{d_r}\right)}{2 \bullet \pi \bullet \lambda_s \bullet H} \tag{9}$$

The front thickness is presented in Fig. 20. A similar growth of thickness as in the case of solid fractions is observed. After about 500 s the growth curve flattens out.

4.4. Uncertainties in the results performed by image processing

The maximum error in the case of both image data analysis method is a function of many different parameters. (Optical, geometrical etc.). However, the quality of presented photos will have the most influence on total error. That quality has been thoroughly analyzed by the special MATLAB algorithm. Generally, the error connected with the photo quality can be assumed as maximum value from MAE (<6.5%).

However, in case of second methods it is possible also to calculate uncertainties from the calibration of images. The solid front thickness has been measured physically using commercial CAD software (see Fig. 21). It has been calculated from simple proportions. At first, it has been measured dimension of copper tube with knowing diameter (6 mm), then the other results were linearly rescaled with respect to the obtained reference result. The physical measurements and estimates from MATLAB algorithm have been shown in Table 8 with percentage error while Fig. 22 presents the error bars of calculated measurements.

The most pessimistic error is no larger than ±7%.

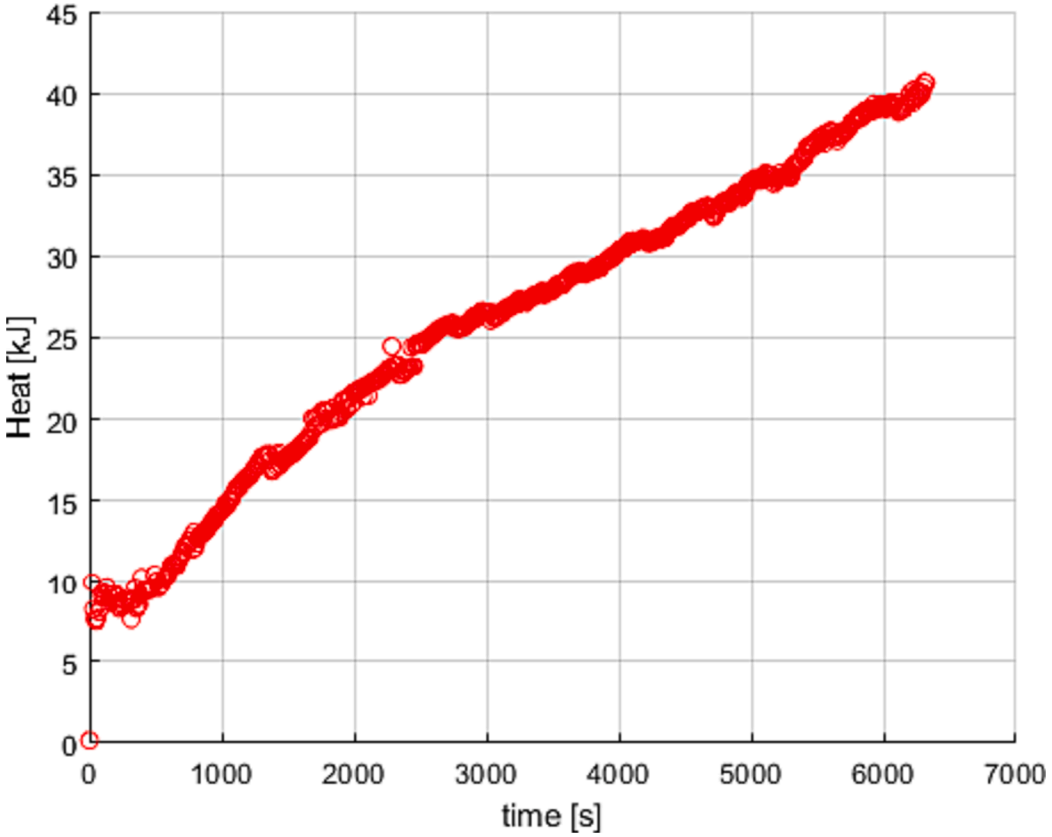

Fig. 17. Heat released during solidification of RT18HC as a time function.

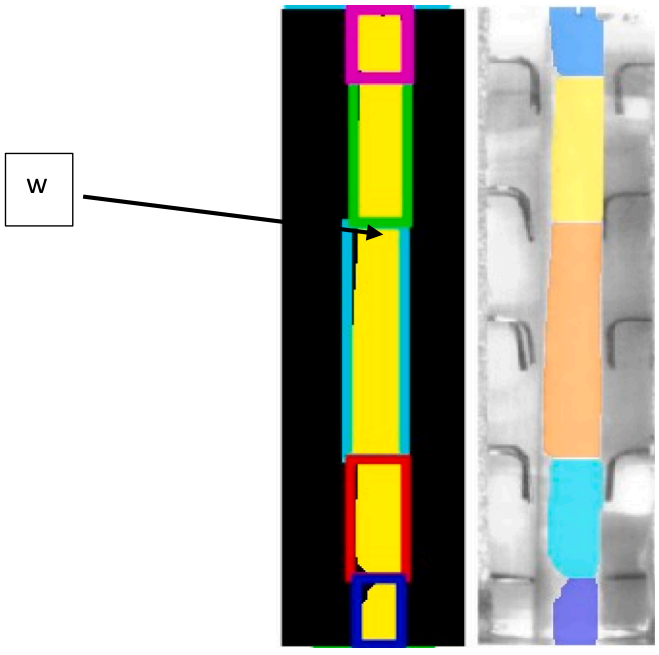

Fig. 18. The example of images with labelled regions of solid fraction: at the right binary image; at the right image in grayscale.

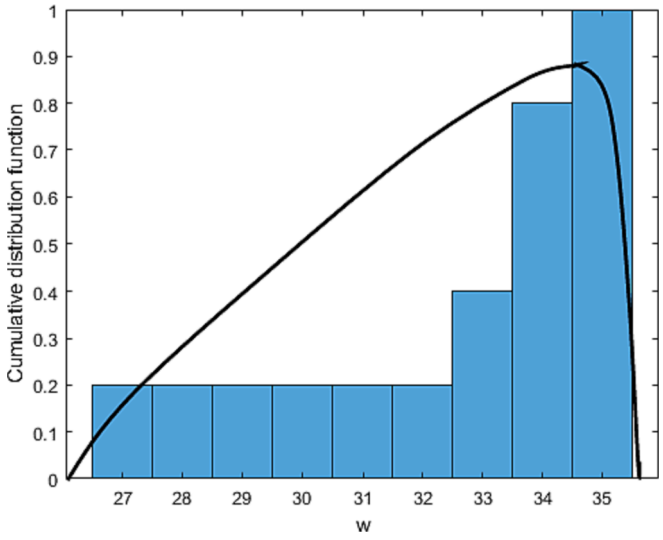

Fig. 19. Cumulative distribution function for front width of solidified layer.

5. Heat transfer analysis

In the case of convective heat transfer thermal resistance, the heat transfer coefficient has been calculated by Woon-Shing Yeung correlation [40]:

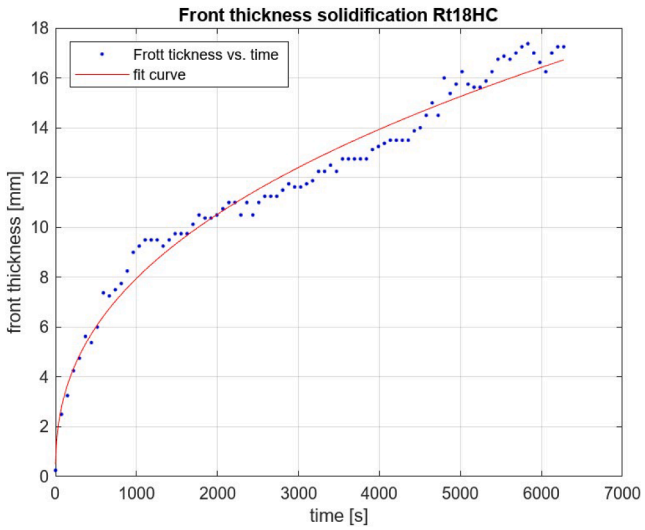

Fig. 20. The front thickness of PCM as a time function.

$$R_{conv} = \frac{1}{h \bullet \pi d_i \bullet H} \tag{10}$$

$$h = 0.322 \bullet Ra^{0.269} \tag{11}$$

$$R_{tot} = R_{cond} + R_{conv} \tag{12}$$

$$Q_i = (T_s - T_w)/R_{total} \tag{13}$$

$$Q = \sum Q_i \tag{14}$$

The total thermal resistance has been presented on Fig. 23. It is important to note that the decrease of convective thermal resistance is connected with the increase in heat transfer coefficient by the growth of a solid layer over the tube. The thermal resistance of the solid layer grows throughout the process. However, the total resistance decreases because of the increase of heat transfer area and the larger influence of convective thermal resistance.

Finally, from heat flux, similar to the previously presented methodology, it is possible to calculate the amount of heat released by PCM during solidification. The results are different not more than 20% (see

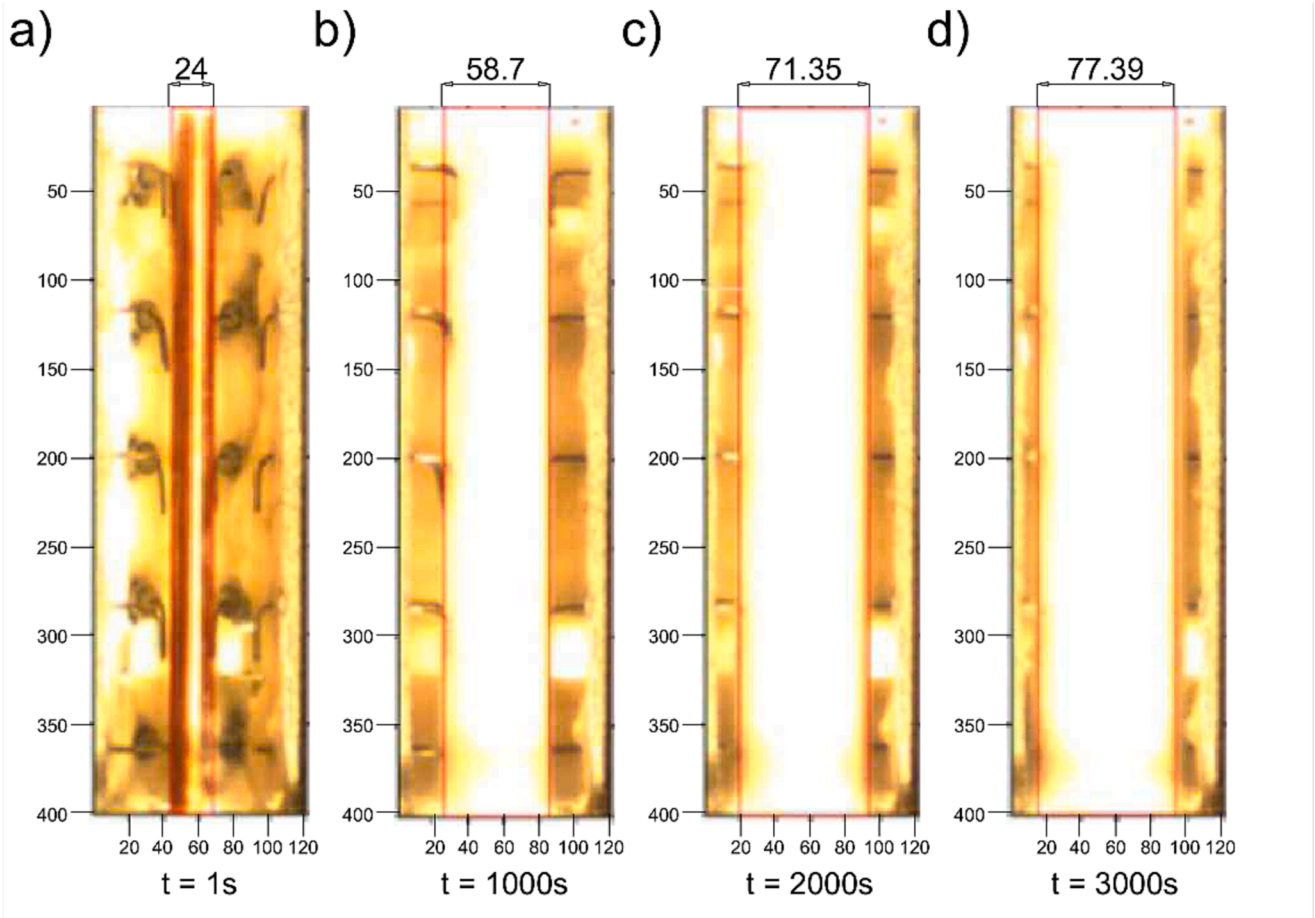

Fig. 21. Physical measurements of solidification front (in mm): a) solidification front after 3000 s, b) solidification front after 2000 s, c) solidification front after 1000 s, d) solidification front after 1 s.

Table 8
Comparison of solid front thickness measured physically and using the MATLAB algorithm.

Time	t = 1000 s			t = 2000 s			t = 3000 s		
Measurement	Physical	Algorithm	Error%	Physical	Algorithm	Error%	Physical	Algorithm	Error%
Solid front thickness [mm]	7.34	8.4	±6.3%	8.92	9.78	±4.4%	9.67	10.93	5.76%

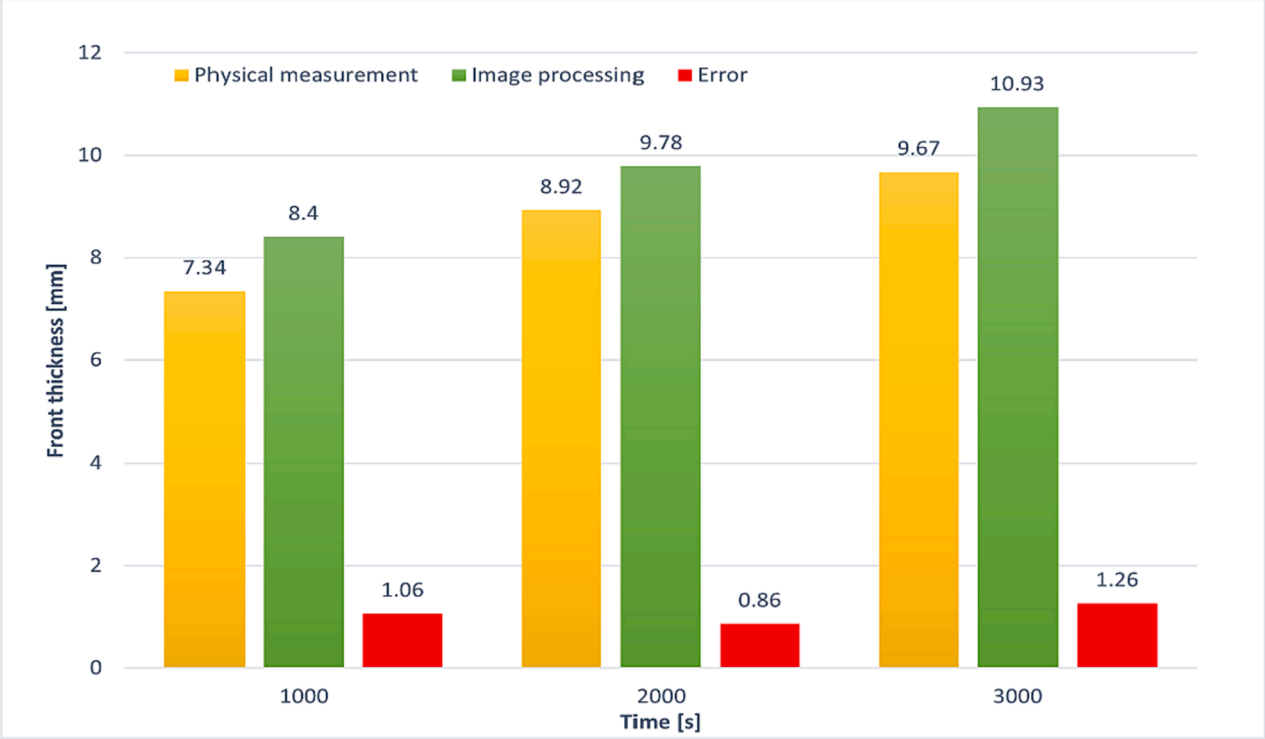

Fig. 22. Error Analysis of Solidification front thickness at different time steps.

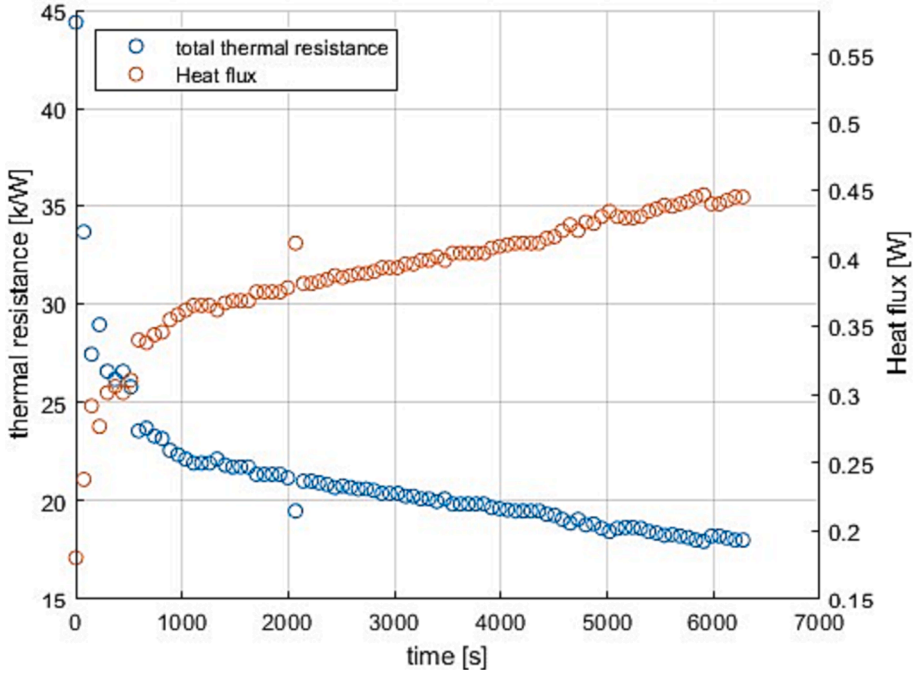

Fig. 23. The total thermal resistance and the heat flux as a function of time during solidification of RT18HC.

Fig. 24).

6. Theoretical model

One of the most common designs of PCM thermal energy storage is a shell-tube configuration. In order to optimally determine the distribution of the tubes in shell, it is necessary to determine the effective phase change front region thickness. The effective front region thickness (δ) could be defined as a thickness (δ) of melting/solidifying layer of PCM for assumed working time and for particular geometry of TES.

As discussed in the introduction, very few studies on thickness of solidification front e.g. [26,27] have been reported effectively and the authors couldn't find any proper literature (experimental) data of thickness front. Which leads the authors to develop and propose a simplified semi-empirical model to calculate the thickness of solidification front. One thing should be noted here that given model has also

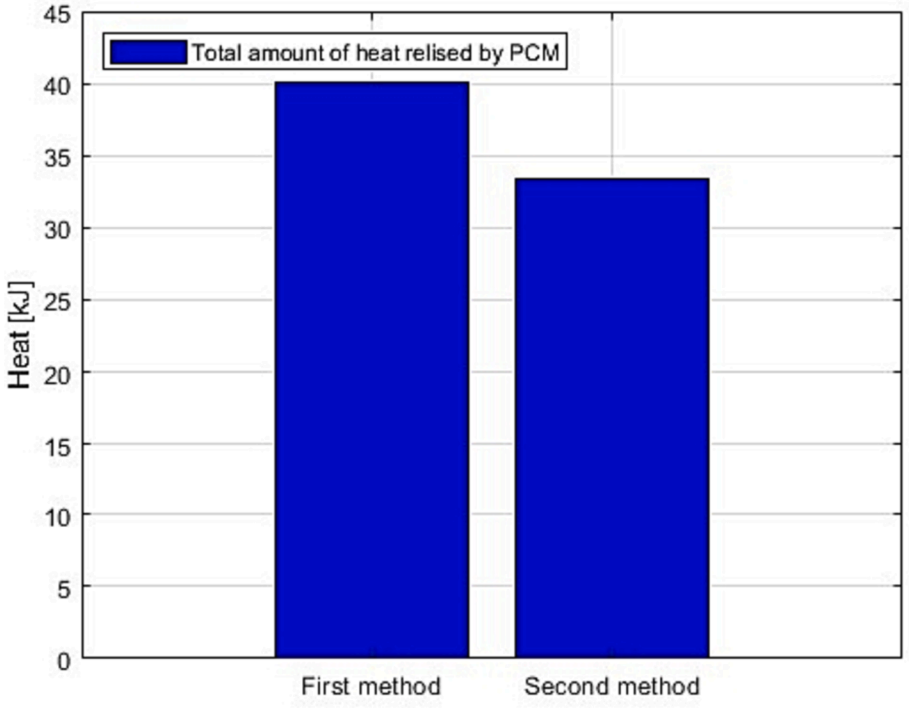

Fig. 24. The comparison of calculation results for the amount of heat released by PCM during solidification by used methodology.

been presented by authors in [41] with a whole different perspective and methodology to optimize the TES geometry.

In general, the following assumptions were made to create an analytical model reflecting the physics of the phase transition phenomenon during the solidification process:

- The influence of axial heat flux on the heat transfer rate was omitted, the dominance of radial heat flux was assumed.
- A substitute thermal conductivity coefficient λ_z was assumed, which is a function of the average conductivity coefficient for the solid phase of a phase-change material (at a temperature as close as possible to the phase transition point) and the product of the coefficient dependent on free convection.

$$\lambda_z = \lambda \bullet \varepsilon_k \tag{15}$$

$$\varepsilon_k = C \bullet Ra^n \tag{16}$$

- The heat flux supplied to the phase-change material is equal to the sum of the sensible and latent heat fluxes accumulating in the body, heat losses to the environment are omitted here.
- The average value of the specific heat for the liquid phase is temperature independent of temperature.
- In order to determine the properties of the fluid for the determination of the Rayleigh number, it is assumed to use the so-called characteristic temperature T_{ch} defined as below.

$$T_{ch} = \frac{T_w + T_m}{2} \tag{17}$$

Fig. 25 shows the phenomenon that facilitates the interpretation of the adopted assumptions.

D_t - diameter of the cylinder (tubes).

D_{sh} – inner diameter of the thermal storage tank, or replacement diameter for hexagonal shape.

On the basis of the following considerations, the following reasoning was carried out in order to determine analytically the equation necessary to determine the so-called thickness of the front undergoing phase transformation.

$$\dot{Q} = \dot{Q}_j + \dot{Q}_u \tag{18}$$

For small "thicknesses" of the PCM layer, it is possible to treat the thermal resistance in a simplified form, as for a flat partition. Assuming the dominance of the heat flux transmitted perpendicular to the heat transfer surface (omission of the axial heat flux) and the constant value of the thermal conductivity coefficient of the phase-change material.

$$\dot{Q} = \dot{m} \bullet c \bullet \Delta T \tag{19}$$

After using the basics of average heat transfer energy and the definition of rate of heat conduction Eq. (18) can be modified as given:

$$\frac{m_s \bullet cp_s \bullet \Delta T}{t} + \frac{m_s h_s}{t} = \frac{\lambda_z}{\delta} \bullet A \bullet \Delta T \tag{20}$$

After simplifying Eq. (20) based on assumptions made earlier, Eq. (21) is obtained:

$$1 + \frac{h_s \bullet m_s}{m_s \bullet cp_s \bullet \Delta T} = \frac{\lambda \bullet \varepsilon_k \bullet A \bullet \Delta T \bullet t}{\delta \bullet \rho_s \bullet V \bullet cp_s \bullet \Delta T} \tag{21}$$

Using the definition of thermal diffusivity α given by the relation:

$$\alpha = \frac{\lambda}{\rho \bullet cp_s} \tag{22}$$

$$1 + \frac{h_{ls}}{cp_s \bullet \Delta T} = \frac{\alpha \bullet \varepsilon_k \bullet \Delta T \bullet t}{\delta \bullet \Delta T \bullet L^*} \tag{23}$$

Where L^* is introduced as characteristic length and can be defined in terms of storage unit characteristic diameter as following:

$$L^* = \frac{V}{A} = \frac{D_s - D_t}{2} \tag{24}$$

Now Eq. (23) has been rearranged to introduce dimensionless parameters named as Stefan number Raleigh number and Fourier number given by the following relations:

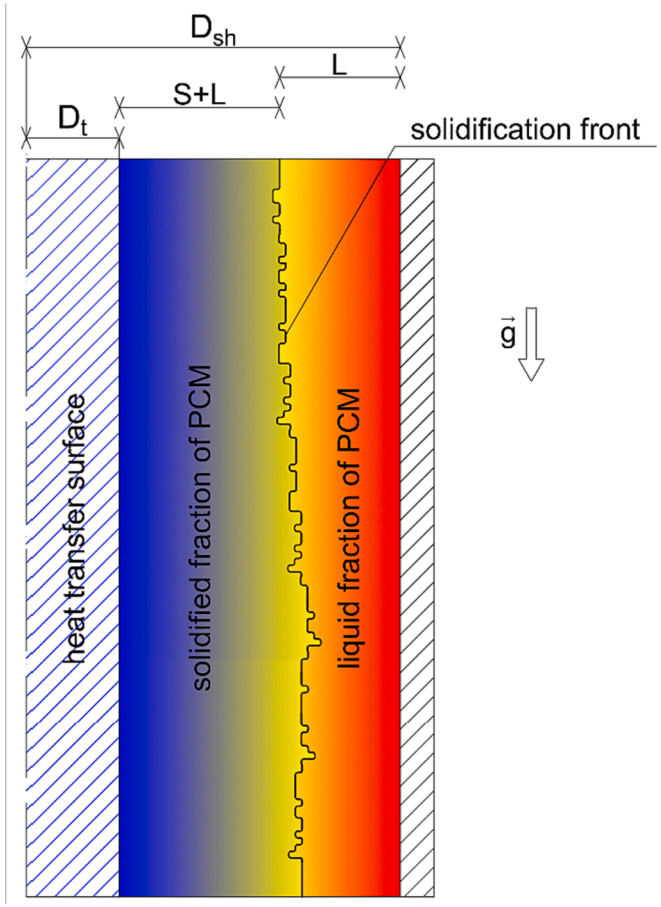

Fig. 25. Schematic representation of solidification process occurring within a cylindrical shell with highlighted solidification front (blue and red colours represent actual temperature levels of PCM). (For interpretation of the references to color in this figure legend, the reader is referred to the web version of this article.)

$$Ste_s = \frac{Cp_s \bullet \Delta T}{h_s} \tag{25}$$

$$F_o = \frac{\alpha \bullet t}{L^{*2}} \tag{26}$$

$$\mathrm{Ra} = \frac{g \bullet \beta \bullet \Delta T \bullet L^{*3}}{\alpha \bullet \eta} \tag{27}$$

Ultimately, the following equation is obtained from Eq. (24).

$$\frac{\delta}{L^*} = \frac{C \bullet Ra^n \bullet F_o \bullet Ste_s}{(Ste_s + 1)^1} \tag{28}$$

It should also be noted that for the Rayleigh number, a geometric dimension should be used that has a direct impact on the rate of free convection, for the case of a heat transfer surface in the form of a cylindrical tube oriented perpendicular to the ground, this dimension for the heat transfer surface in the form of a cylindrical tube/vertical plate can be defined as the height of the H module.

For different working mediums (phase-change substances), the need to determine additional matching factors should be taken into account. Taking this fact into account, the general formula takes the following form:

$$\frac{\delta}{L^*} = \frac{C \bullet Ra^n \bullet Fo^m \bullet Ste_s{}^l}{(Ste_s + 1)^k} \tag{29}$$

Where n, m, l, and k are matching coefficients.

If there is a significant difference in the value of the heat transfer coefficient depending on the temperature of the working medium. The above approach should be modified using the following reasoning (see Fig. 26):

b – is the coefficient of proportionality for the equation determining the average value of the conductivity coefficient of a phase-change material

$$\lambda_m = \frac{\lambda_1 + \lambda_2}{2} = \lambda \bullet \left[1 + b \bullet \left(\frac{T_w + T_m}{2}\right)\right] \tag{30}$$

Factor "b" will depend on the equilibrium between the liquid and solid phases.

The above solution will also be valid for plate geometry after appropriate modification of the dimension's characteristic of the Rayleigh and Fourier numbers. However, a solution extended by a general definition of thermal resistance for a cylindrical partition is also worth presenting:

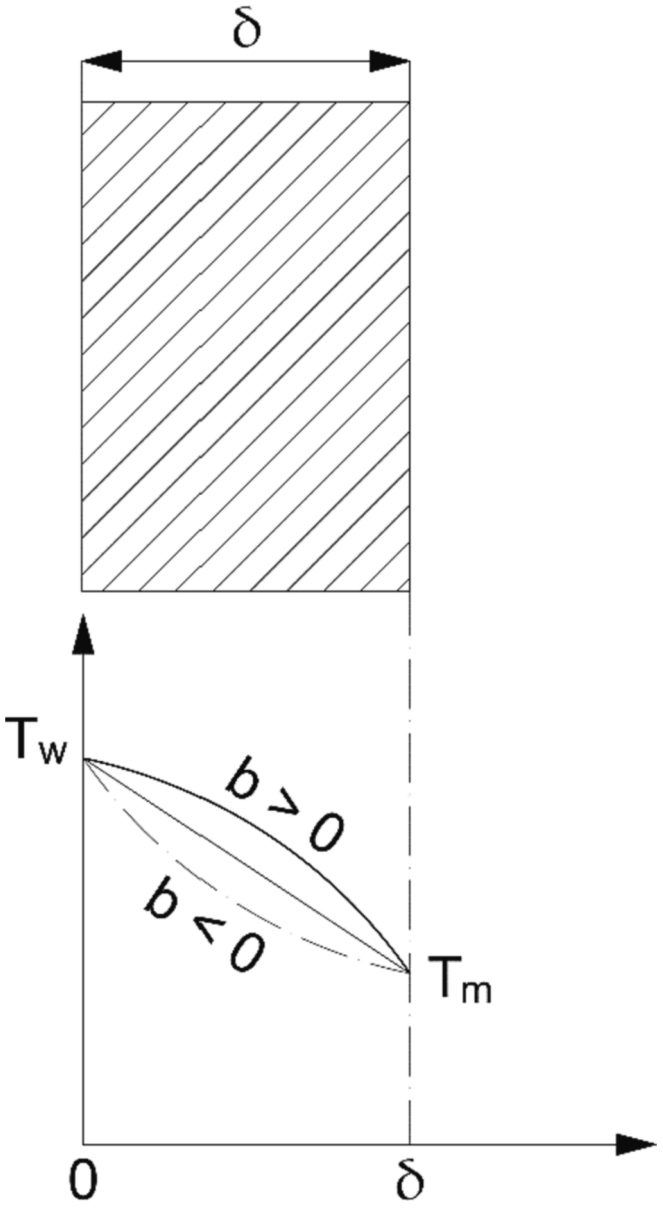

Fig. 26. Schematic representation of temperature profile.

$$\frac{m_s \bullet cp_s \bullet \Delta T}{t} + \frac{m_s h_s}{t} = \frac{\lambda_z}{\delta} \bullet \frac{D_s - d_r}{\ln\left(\frac{D_s}{d_r}\right)} \bullet \Delta T \tag{31}$$

After repeating same procedural step, the thickness δ of the solidification front can be determined from the dependencies given by equation (32).

$$\delta = \frac{C \bullet Ra^n \bullet Fo^m \bullet Ste_s{}^l}{\pi \bullet \ln\left(\frac{D_s}{d_r}\right) \bullet (D_s - d_r) \bullet (Ste_s + 1)^k} \bullet H \tag{32}$$

Where n, m, l, and k are already defined as matching coefficients.

As discussed earlier, the unavailability of proper literature or experimental data for front thickness was also the a motivating factor to calculate front thickness by image processing. We use our own front thickness data calculated earlier by image processing as reference data to calculate the unknown coefficients by applying the least square fitting method on our proposed theoretical model. To follow the procedure, calculations were performed on Eqn 32 and in geometry presented in Fig. 25. Dimensions of storage unit were taken as height (H) 165 mm, inner diameter (D_s) of shell 40 mm, while diameter of the tube (d_s) was 10 mm. RT18HC was selected as storage material (PCM) whose thermodynamic properties are already mentioned in Table 5. The initial temperature T_i was recorded as 298.15 K while constant wall temperature T_w adjusted to 283.65 K. Finally, fitted curve presented in Fig. 27 whereas values of calculated coefficients are given as under. Moreover, value of R-squared (R^2) is 0.9545 which is near to 1 which shows the goodness of fit as high, also the low values of MSE and RMSE validate the model fitting.

C	n	m	l	k
0.217722	0.363073	0.439694	0.710398	0.272131

Since, the image analysis technique presented in this paper is very novel it leads to this nonlinear behavior of front thickness. Furthermore, more experimental results will be required with a more sophisticated experimental setup to generalize our model. Which is currently not possible because of large financial implications.

Therefore, we aim to do more intensive research on image data analysis techniques to obtain more accurate results for thickness of solidification front and solid fraction in future. Which ultimately will enable us to present a concrete and detailed parametric and thermal analysis of our model.

7. Conclusions

This article presents a new methodology based on image analysis to calculate the solid fraction of RT18HC and the solid front thickness in symmetrical shell and tube storage unit for further analysis of solidification process. Along with it a novel, simplified, semi-empirical theoretical model has been proposed to calculate the thickness of solidification front.

The main idea of the algorithm is to label the region of solidification and use statistical functions to calculate the dimensions of the solidification front over time. First of all, the quality of the photos has been checked to confirm the usefulness of image database. To measure the solid fraction changes during the solidification process two different methods have been utilized. Both of them are based on utilizing images only in black and white (binary image). Both of presented methodologies have shown similar results of total heat flux released by PCM during process. However, the second methodology gave an experimental database to develop the proposed analytical model. Key findings of the study are listed below:

1. The new experimental database with solid fraction and solid front thickness as a time function during solidification of RT18HC has been obtained. This database shown that solidification process was very fast. 40% of the solid fraction was obtained during the first1000 s while the rest of the process was completed in almost 6500 s.
2. The possibility of using a simple, non-invasive method to track the solid/melting front change was confirmed during this study. As

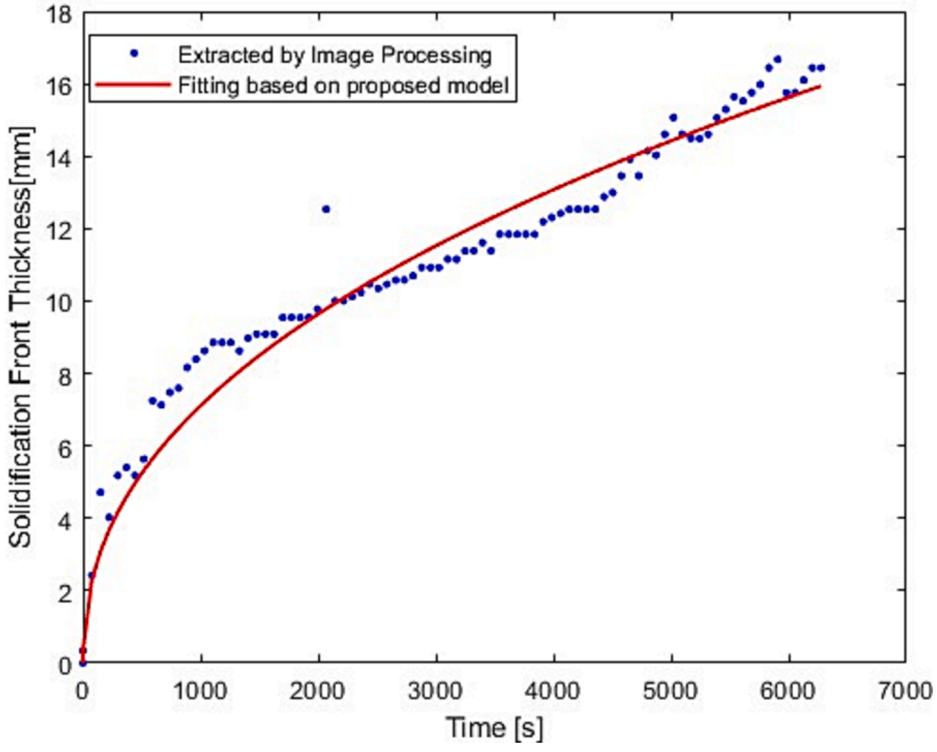

Fig. 27. Curve Fitting Based on Proposed Model to Calculate Unknown Coefficients.

compared to other literature findings this process occurred entirely automatically through an in-house calculating algorithm.
3. The error of the first of the methods was calculated to be less than 7% throughout the entire process.
4. Both of the used image data analysis techniques provide valuable experimental data which could be used to validate numerical calculations. There is less than 20% difference in average in the total amount of heat released by PCM calculated by the first and second method which can be improved significantly by upgrading the equipment and experimental setup.
5. The second method provides the data for heat transfer rate analysis between the solid and liquid PCM. It is because heat conduction and heat convection mechanism are occurring at the interface of solid/liquid phase. This means that the geometry of interface is crucial for heat transfer.
6. Influences of heat transfer area at total thermal resistance and the heat flux during solidification of RT18HC has been confirmed. The thermal resistance of the solid layer is growing during the process, but due to the increase in heat transfer area by the growth of a solid layer over the tube, a decrease of convective thermal resistance can be observed. Such an effect would not be present in case of plate geometry.
7. A novel, simplified, semi-empirical theoretical model has been proposed to calculate the thickness of solidification front as a function of time. This model will be valid for plate geometry after appropriate modification of the dimension's characteristic of the Rayleigh and Fourier numbers. Unknown coefficients have been calculated using nonlinear regression, but it should not be generalized at the moment because of lack of experimental data, which could be acquired by more experiments and could be obtained more accurately with upgraded experimental lab.

Therefore, authors aim to perform more intensive research on image data analysis techniques to get more accurate results to study the applications of given technique on different geometries. Special attention will be focused on mushy zone influences at amount of solid/melting fraction during phase change. This would ultimately enable the authors to present a more concrete and detailed parametric and thermal analysis of our model. For that purpose, other color scales, beside binary would be utilized.

Declaration of Competing Interest

The authors declare that they have no known competing financial interests or personal relationships that could have appeared to influence the work reported in this paper.

Data availability

Data will be made available on request.

Acknowledgment

This research work was supported by the National Centre for Research and Development, Poland (Project No. LIDER/4/0008/L-9/17/NCBR/2018). Special thanks to Mr Przemysław Kozak and PhD Maciej Fabrykiewicz who were LIDER project team members.

References

[1] R. Viskanta, Phase-change heat transfer, in: Solar Heat Storage: Latent Heat Material: Volume I: Background and Scientific Principles, 2018. https://doi.org/10.1201/9781351076753.
[2] F.B. Cheung, M. Epstein, Solidification and melting in fluid flow, Adv. Transp. Processes. 3 (1984).
[3] M. Saqib, R. Andrzejczyk, A review of phase change materials and heat enhancement methodologies, Wires Energy Environ. 12 (2022) e467, https://doi.org/10.1002/wene.467.
[4] M. Kenisarin, K. Mahkamov, Solar energy storage using phase change materials, Renew. Sustain. Energy Rev. 11 (2007) 1913–1965, https://doi.org/10.1016/J.RSER.2006.05.005.
[5] H. Jouhara, A. Żabnieńska-Góra, N. Khordehgah, D. Ahmad, T. Lipinski, Latent thermal energy storage technologies and applications: A review, Int. J. Thermofluids. 5–6 (2020), 100039, https://doi.org/10.1016/j.ijft.2020.100039.
[6] C. Liu, D. Groulx, Experimental study of the phase change heat transfer inside a horizontal cylindrical latent heat energy storage system, Int. J. Therm. Sci. 82 (2014), https://doi.org/10.1016/j.ijthermalsci.2014.03.014.
[7] M. Avci, M.Y. Yazici, Experimental study of thermal energy storage characteristics of a paraffin in a horizontal tube-in-shell storage unit, Energy Convers Manag. 73 (2013) 271–277, https://doi.org/10.1016/J.ENCONMAN.2013.04.030.
[8] P. Lamberg, Approximate analytical model for two-phase solidification problem in a finned phase-change material storage, Appl Energy. 77 (2004) 131–152, https://doi.org/10.1016/S0306-2619(03)00106-5.
[9] A.H. Mosaffa, F. Talati, H. Basirat Tabrizi, M.A. Rosen, Analytical modeling of PCM solidification in a shell and tube finned thermal storage for air conditioning systems, Energy Build. 49 (2012), https://doi.org/10.1016/j.enbuild.2012.02.053.
[10] A.R. Al-Obaidi, Investigation of thermal flow structure and performance heat transfer in three-dimensional circular pipe using twisted tape based on Taguchi method analysis, Heat Transf.. 51 (2022) 1649–1667, https://doi.org/10.1002/htj.22368.
[11] A.R. Al-Obaidi, Characterization of internal thermohydraulic flow and heat transfer improvement in a three-dimensional circular corrugated tube surfaces based on numerical simulation and design of experiment, Heat Transf. 51 (2022) 4688–4713, https://doi.org/10.1002/htj.22519.
[12] A.R. Al-Obaidi, Thermal flow and heat performance analyses in circular pipe using different twisted tape parameters based on design of experiments, Heat Transf. 51 (2022) 7202–7232, https://doi.org/10.1002/htj.22641.
[13] A. Ramadhan Al-Obaidi, I. Chaer, Study of the flow characteristics, pressure drop and augmentation of heat performance in a horizontal pipe with and without twisted tape inserts, Case Studies, Therm. Eng. 25 (2021), 100964, https://doi.org/10.1016/J.CSITE.2021.100964.
[14] A.M. Sefidan, A. Sojoudi, S.C. Saha, M. Cholette, Multi-layer PCM solidification in a finned triplex tube considering natural convection, Appl. Therm. Eng. 123 (2017) 901–916, https://doi.org/10.1016/J.APPLTHERMALENG.2017.05.156.
[15] M. Esapour, A. Hamzehnezhad, A.A. Rabienataj Darzi, M. Jourabian, Melting and solidification of PCM embedded in porous metal foam in horizontal multi-tube heat storage system, Energy Convers. Manag. 171 (2018) 398–410, https://doi.org/10.1016/J.ENCONMAN.2018.05.086.
[16] S. Loem, T. Deethayat, A. Asanakham, T. Kiatsiriroat, Study on phase change material thermal characteristics during air charging/discharging for energy saving of air-conditioner, Heat Mass Transf. 56 (2020) 2121–2133, https://doi.org/10.1007/s00231-020-02839-4.
[17] M.H. Jahangir, S.M.E. Razavi, A. Kasaeian, H. Sarrafha, Comparative study on thermal performance of an air based photovoltaic/thermal system integrated with different phase change materials, Sol. Energy. 208 (2020) 1078–1090, https://doi.org/10.1016/j.solener.2020.08.056.
[18] M. Rogowski, R. Andrzejczyk, Recent advances of selected passive heat transfer intensification methods for phase change material-based latent heat energy storage units: A review, Int. Commun. Heat Mass Transf. 144 (2023), 106795, https://doi.org/10.1016/j.icheatmasstransfer.2023.106795.
[19] X. Wang, Y. Fautrelle, An investigation of the influence of natural convection on tin solidification using a quasi two-dimensional experimental benchmark, Int. J. Heat Mass Transf. 52 (2009) 5624–5633, https://doi.org/10.1016/J.IJHEATMASSTRANSFER.2009.05.030.
[20] J.P. Garandet, C. Salvi, Identification of furnace thermal characteristics from resistance measurements, Int. J. Heat Mass Transf. 45 (2002) 1045–1054, https://doi.org/10.1016/S0017-9310(01)00207-1.
[21] H. Zhang, M. Charmchi, D. Veilleux, M. Faghri, Numerical and Experimental Investigation of Melting in the Presence of a Magnetic Field: Simulation of Low-Gravity Environment, J. Heat Transf. 129 (2007) 568–576, https://doi.org/10.1115/1.2709961.
[22] R. Derebail, J.N. Koster, Visualization study of melting and solidification in convecting hypoeutectic Ga-In alloy, Int. J. Heat Mass Transf. 41 (1998) 2537–2548, https://doi.org/10.1016/S0017-9310(97)00145-2.
[23] E. Assis, L. Katsman, G. Ziskind, R. Letan, Numerical and experimental study of melting in a spherical shell, Int. J. Heat Mass Transf. 50 (2007) 1790–1804, https://doi.org/10.1016/j.ijheatmasstransfer.2006.10.007.
[24] H. Shmueli, G. Ziskind, R. Letan, Melting in a vertical cylindrical tube: Numerical investigation and comparison with experiments, Int. J. Heat Mass Transf. 53 (2010) 4082–4091, https://doi.org/10.1016/J.IJHEATMASSTRANSFER.2010.05.028.
[25] M. Pinelli, S. Piva, Solid/Liquid Phase Change in Presence of Natural Convection: A Thermal Energy Storage Case Study, J. Energy Resour. Technol. 125 (2003) 190–198, https://doi.org/10.1115/1.1591204.
[26] B. Weigand, Z. Lipnicki, Development of the contact layer and its role in the phase change process, Int. J. Heat Mass Transf. 93 (2016) 1082–1088, https://doi.org/10.1016/J.IJHEATMASSTRANSFER.2015.10.070.
[27] M. Gortych, Z. Lipnicki, B. Weigand, An experimental and theoretical study of the solidification process of phase change materials in a horizontal annular enclosure, Appl. Therm. Eng. 161 (2019), 114140, https://doi.org/10.1016/J.APPLTHERMALENG.2019.114140.

[28] Query Link - Web Of Science, (n.d.). https://www.webofscience.com/wos/woscc/summary/86d0fc63-b739-4b75-a272-668f6f0a89bd-88f180d0/relevance/1 (accessed May 10, 2023).
[29] M. Azad, D. Groulx, A. Donaldson, Solidification of phase change materials in horizontal annuli, J. Energy Storage. 57 (2023), 106308, https://doi.org/10.1016/J.EST.2022.106308.
[30] Rubitherm, https://www.rubitherm.eu/media/products/datasheets/Techdata_-RT18HC_EN_09102020.PDF, (n.d.). https://www.rubitherm.eu/media/products/datasheets/Techdata_-RT18HC_EN_09102020.PDF (accessed February 1, 2023).
[31] O. Nnaemeka, E. Bibeau, Turning Winter Into Summer: Operating a Truck With B100 Biodiesel All Year Round in Cold Regions, in: CSBE/SCGAB 2017 Annual Conference, 2017, pp. 1–11.
[32] A. Solé, L. Miró, C. Barreneche, I. Martorell, L.F. Cabeza, Review of the T-history method to determine thermophysical properties of phase change materials (PCM), Renew. Sustain. Energy Rev. 26 (2013) 425–436, https://doi.org/10.1016/J.RSER.2013.05.066.
[33] Z. Wang, A.C. Bovik, A universal image quality index, IEEE Signal Process Lett. (2002), https://doi.org/10.1109/97.995823.
[34] W. Kim, D.S. Kim, Gradient shadow pattern reveals refractive index of liquid, Sci. Rep. (2016), https://doi.org/10.1038/srep28191.
[35] D. Heim, M. Krempski-Smejda, P.R. Dellicompagni, D. Knera, A. Wieprzkowicz, J. Franco, Dynamics of melting process in phase change material windows determined based on direct light transmission, Energies (basel). (2021), https://doi.org/10.3390/en14030721.
[36] M. Azad, D. Groulx, A. Donaldson, Natural convection onset during melting of phase change materials: Part I - Effects of the geometry, Stefan number, and degree of subcooling, Int. J. Therm. Sci. (2021), https://doi.org/10.1016/j.ijthermalsci.2021.107180.
[37] M. Avci, M.Y. Yazici, Experimental study of thermal energy storage characteristics of a paraffin in a horizontal tube-in-shell storage unit, Energy Convers. Manag. (2013), https://doi.org/10.1016/j.enconman.2013.04.030.
[38] D.S. Mehta, K. Solanki, M.K. Rathod, J. Banerjee, Thermal performance of shell and tube latent heat storage unit: Comparative assessment of horizontal and vertical orientation, J Energy Storage. (2019), https://doi.org/10.1016/j.est.2019.03.007.
[39] Inc. The MathWorks, Image Processing Toolbox™ Reference, 2022.
[40] W.S. Yeung, Analysis of natural convection in a closed vertical annulus, Int. Commun. Heat Mass Transf. (1989), https://doi.org/10.1016/0735-1933(89)90092-4.
[41] R. Andrzejczyk, M. Saqib, T. Kowalcyzk, H.M. Ali, Study on effective front region thickness of PCM in thermal energy storage using a novel semi-theoretical model, Int. Commun. Heat Mass Transf. 146 (2023), 106901, https://doi.org/10.1016/J.ICHEATMASSTRANSFER.2023.106901.